Journal of Computational Physics **150,** 40–75 (1999)
Article ID jcph.1998.6163, available online at http://www.idealibrary.com on IDEAL®

A Conservative Finite-Volume Second-Order-Accurate Projection Method on Hybrid Unstructured Grids

Marcelo H. Kobayashi,* José M. C. Pereira,† and José C. F. Pereira‡

Department of Mechanical Engineering/LASEF, Instituto Superior Técnico/Technical University of Lisbon, Av. Rovisco Pais, 1049-001 Lisbon, Portugal
E-mail: *marcelo@navier.ist.utl.pt, †zeman@navier.ist.utl.pt, and ‡jose@pomar.ist.utl.pt

Received May 6, 1998; revised December 3, 1998

This paper describes a finite volume discretization method to compute steady, two-dimensional incompressible viscous recirculating flows using hybrid unstructured meshes, composed of triangles and quadrilaterals. However, the proposed formulation is not restricted to these topologies.

The new method includes a second-order least squares scheme for convection discretization, and a fractional step projection method based on a staggered grid arrangement for pressure velocity coupling. Numerical results are reported to demonstrate the robustness, second-order accuracy, and flexibility of the proposed method.

To the authors' knowledge, this paper represents the first general unstructured grid finite volume method to achieve full second-order accuracy for the steady incompressible 2D version of Navier–Stokes equations.

Key Words: viscous flow; incompressible; projection methods; unstructured hybrid grids.

1. INTRODUCTION

The numerical integration of the Navier–Stokes equations, for incompressible fluid flow in primitive variable formulation, faces the problem of the pressure–velocity coupling. This problem has been overcome in the framework of finite differences or finite volume method by several classical methods and mesh collocation arrangements for the dependent variables; see, for example, [1–5]. Extensions of these methods are straightforward for structured curvilinear orthogonal or non-orthogonal grids; see, for example, [6]. However, for unstructured grids, the numerical methods to achieve pressure–velocity coupling are less well documented in the open literature and most of the reported works employ versions of the SIMPLE algorithm for collocated meshes.

0021-9991/99 $30.00

The Harlow–Welch algorithm [1] constrains the velocity field into zero divergence by coupling the continuity and momentum equations via a pressure Poisson equation. The requirement for artificial boundary conditions for the pressure equation may not be in agreement with the requirement of velocity boundary conditions for the Navier–Stokes equations [7]. Chorin [3] proposed an explicit and dissipative artificial compressibility method by combining the continuity equation and an artificial state equation to obtain the pressure field. Patankar and Spalding [4] proposed the family of semi-implicit pressure-linked equations that impose the incompressibility constraint via a Poisson equation for pressure correction.

The projection methods [8, 9] are based in the Hodge decomposition in Hilbert spaces where the divergence vanishes through the orthogonal projection in the vector space of zero divergence. This projection is made using discrete operators for divergence and gradient (its skew adjoint).

First- and second-order-accurate versions of the projection method have been proposed in the framework of finite differences using structured grids. Van Kan [10] has proposed a version of the projection method for structured orthogonal staggered grids using the skew adjoint of the discrete divergence operator as discrete gradient operator. Bell *et al.* [11] have proposed a projection method for structured Cartesian staggered meshes in which the projection was attained by a Galerkin procedure. Moreover, the gradient discretization was used to obtain the skew adjoint of the divergence operator. A generalization of this method for structured non-orthogonal mesh arrangements was proposed by Bell *et al.* [12]. Also, the condition of zero divergence has been relaxed by Almgren *et al.* [13].

For unstructured grids, Guermond and Quartapelle [14] have proposed, in the framework of the finite element method, a projection method for triangular meshes. Also in the context of finite elements, Gresho [15, 16] has derived several types of projection methods which included a complete discussion of the related theoretical aspects of the methods.

The present paper presents a conservative finite volume projection method for the solution of the incompressible Navier–Stokes equations. The method is based on a hybrid unstructured mesh composed of, but not restricted to, triangles and quadrilaterals that may be mixed in the computational domain. It uses a staggered grid arrangement, which is a generalization for hybrid unstructured grids of the ICED-ALE arrangement [2]. The pressure field is computed in a way that averts generating a checkerboard distribution associated with the ICED-ALE staggering arrangement for quadrilaterals. The overall method is, to the authors knowledge, the first finite-volume method based on a hybrid unstructured grid to attain full second-order accuracy in the computations of incompressible fluid flows.

The accuracy and the stability of the upwind least squares scheme (ULSS) are analyzed within the present framework. Finally, the accuracy and the robustness of the ensuing method are assessed. This is done by comparing our solutions against either known analytical or standard numerical test case solutions available in the literature.

2. DISCRETIZATION PROCEDURE

The transport equation for a quantity ϕ in the intrinsic form can be written as

$$\frac{\partial \rho\phi}{\partial t} + \operatorname{div}(\rho u\phi - \Gamma_\phi \operatorname{grad}\phi) = S_\phi, \tag{2.1}$$

where u is the velocity vector field, ρ is the density field, Γ_ϕ is the diffusivity of ϕ, and

S_ϕ is the source/sink balance of ϕ. In the present work, by using the finite-volume method, numerical integration of Eq. (2.1) is carried out on an unstructured hybrid grid consisting, in the two-dimensional case, of triangles and quadrilaterals. Other grid topologies are allowed by the formulation but these shapes suffice for most of the applications.

Let σ denote a partition of the domain of interest, $\Omega \subset \mathbf{R}^2$, i.e.,

$$\Omega = \bigcup_{i \in j} \sigma_i, \quad \sigma_i \cap \sigma_j = \varnothing, \quad i \neq j, \quad i, j \in J, \quad \sigma = \{\sigma_i\}_{i \in J},$$

where J is a finite index set; $\sigma_i \in \sigma$ is a control volume. In the present work, each control volume $\sigma_i \in \sigma$ can be either a triangle or a quadrilateral. In the finite-volume approach we start with the integration of Eq. (2.1) over each control volume, so that we seek a solution of Eq. (2.1) in the generalized sense [17].

Given $\tau \in \sigma$, and a time step Δt, it proceeds as

$$\frac{\rho\phi^{n+1} - \rho\phi^n}{\Delta t} m_V(\tau) + \overline{\int_{\partial\tau} (\rho u\phi - \Gamma_\phi \operatorname{grad}\phi) n} = \overline{\int_\tau S_\phi}, \tag{2.2}$$

where $m_V(\tau)$ is the Lebesgue measure of τ, the overbar stands for the temporal average, and we have used the *Gauss Divergence Theorem* to move from an integral over τ to an integral over its boundary $\partial\tau$. Equation (2.2) can be cast in the flux balance form

$$\frac{\rho\phi^{n+1} - \rho\phi^n}{\Delta t} m_V(\tau) + \sum_{i \in \partial\tau} C_i + \sum_{i \in \partial\tau} D_i = S, \tag{2.3}$$

where $\partial\tau$ is the set of faces composing the boundary of τ; S is the average amount of creation/destruction of ϕ over τ; and C_i, D_i stands for the convective and diffusive flux of ϕ over face $i \in \partial\tau$, respectively. In symbols, we have

$$\begin{aligned} C_i &\equiv \overline{\int_i \rho v_n \phi}, \qquad i \in \partial\tau \\ D_i &\equiv \overline{\int_i -\Gamma_\phi \frac{\partial\phi}{\partial n}}, \qquad i \in \partial\tau \\ S &\equiv \overline{\int_\tau S_\phi}, \end{aligned} \tag{2.4}$$

where v_n is the velocity component normal to the face $i \in \partial\tau$ and $\frac{\partial\phi}{\partial n}$ is the derivative in the (exterior) normal direction to the face.

We continue with the description of the discretization of the convective and diffusive fluxes of ϕ.

Convection Discretization Procedure

The ULSS is based on the pointwise reconstruction of the variable ϕ by a piecewise polynomial which, similarly to the essentially non-oscillatory (ENO) scheme [18], is required to be consistent with averaging and of high order of accuracy. These requirements amount to the reconstruction polynomial $R \in \Pi_\sigma(\mathbf{R}^2)$ satisfying:

(a) *consistency*, in the sense that

$$\frac{1}{m_V(\tau)} \int_{\tau} R = \bar{\phi}_{\tau}, \tag{2.5}$$

where $\bar{\phi}_{\tau}$ is the space average value of ϕ over τ;

(b) *high order of accuracy*, in the sense that whenever there is a neighborhood $U \subset \Omega$ where ϕ is regular, we have

$$R(x) = \phi(x) + O(h^r), \qquad x \in U, \tag{2.6}$$

where h is a grid parameter and $r > 1$ is the order of the method, which in the present work is $r = 2$.

The symbol $\Pi_\sigma(\mathbf{R}^2)$ stands for the set of piecewise polynomials in $\mathbf{R}^2$ compatible with a partition σ, i.e., given an element $R \in \Pi_\sigma(\mathbf{R}^2)$ and a set $\tau \in \sigma$, there exists a unique polynomial $p \in \Pi(\mathbf{R}^2)$ such that $p(x) = R(x), x \in \tau$, where $\Pi(\mathbf{R}^2)$ stands for the set of polynomials in $\mathbf{R}^2$. Under the above conditions we proceed with the derivation of R.

We start with the space-averaged values of ϕ stored at the centroids of the control volumes. Then, given a set $\tau \in \sigma$ we approximate the function ϕ over τ by an affine or bilinear function depending on whether τ is a triangle or a quadrilateral, respectively. The polynomial is computed by the least squares approximation of the average values of the function at an appropriate set of neighboring points. Next, we give the details of the procedure for a triangle and a quadrilateral control volume.

τ Is a Triangle

For any pair $(x_1, x_2) \in \tau$ we write

$$R(x_1, x_2; \phi) = \bar{\phi}_{\tau} + a_1 x_1 + a_2 x_2, \tag{2.7}$$

where a_1, a_2 are coefficients to be determined, and (x_1, x_2) are local Cartesian coordinates with origin in the centroid of τ (see Fig. 2.1). We compute the coefficients a_1, a_2 from the

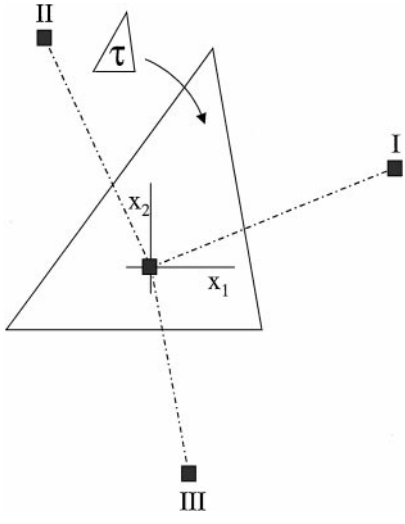

FIG. 2.1. Stencil for convection discretization.

following minimization problem: find a_1, a_2 such that

$$\chi(a_1, a_2) = \sum_{i \in i_\tau} \left(R\left(x_1^i, x_2^i; \phi\right) - \bar{\phi}_i \right)^2 = \sum_{i \in i_\tau} \left(\bar{\phi}_\tau + a_1 x_1^i + a_2 x_2^i - \bar{\phi}_i \right)^2 \tag{2.8}$$

is minimum.

In Eq. (2.8), $i_\tau = \{I, II, III\}$ stands for the set of adjacent control volumes to τ (see Fig. 2.1), and (x_1^i, x_2^i) is the coordinate pair of point $i \in i_\tau$. Solution of this problem is obtained as in the least squares method by solving the set of linear equations resulting from

$$\nabla \chi(a_1, a_2) = 0. \tag{2.9}$$

The solution of the previous equation can be easily shown to be

$$\begin{aligned} a_1 &= \frac{\sum_{i \in i_\tau} (\bar{\phi}_i - \bar{\phi}_\tau) x_1^i \sum_{i \in i_\tau} \left(x_2^i\right)^2 - \sum_{i \in i_\tau} (\bar{\phi}_i - \bar{\phi}_\tau) x_2^i \sum_{i \in i_\tau} x_1^i x_2^i}{\Delta} \\ a_2 &= \frac{\sum_{i \in i_\tau} (\bar{\phi}_i - \bar{\phi}_\tau) x_2^i \sum_{i \in i_\tau} \left(x_1^i\right)^2 - \sum_{i \in i_\tau} (\bar{\phi}_i - \bar{\phi}_\tau) x_1^i \sum_{i \in i_\tau} x_1^i x_2^i}{\Delta}, \end{aligned} \tag{2.10}$$

where Δ is the determinant

$$\Delta = \begin{vmatrix} \sum_{i \in i_\tau} \left(x_1^i\right)^2 & \sum_{i \in i_\tau} x_1^i x_2^i \\ \sum_{i \in i_\tau} x_1^i x_2^i & \sum_{i \in i_\tau} \left(x_2^i\right)^2 \end{vmatrix}. \tag{2.11}$$

Notice that the necessary and sufficient condition for the existence of a unique pair a_1, a_2 is the non-vanishing of the determinant Δ. Next, we prove that it never vanishes in a partition. Writing Δ in expanded form as

$$\Delta = \left(x_1^I x_2^{II} - x_1^{II} x_2^I\right)^2 + \left(x_1^I x_2^{III} - x_1^{III} x_2^I\right)^2 + \left(x_1^{II} x_2^{III} - x_1^{III} x_2^{II}\right)^2 \tag{2.12}$$

we conclude that $\Delta = 0$ is equivalent to

$$\begin{aligned} x_1^I / x_2^I &= x_1^{II} / x_2^{II} \\ x_1^{II} / x_2^{II} &= x_1^{III} / x_2^{III} \\ x_1^{III} / x_2^{III} &= x_1^I / x_2^I. \end{aligned} \tag{2.13}$$

Hence, Δ vanishes if and only if the four centroids, the centroid of τ and those of its three adjacent neighbors, lie over one and the same straight line. Since this cannot occur in any partition we conclude the existence and uniqueness of the coefficients a_1, a_2.

We proceed by showing that R satisfies the proposed conditions of consistency and of high order of accuracy. Consistency follows at once from the fact that the origin of the local coordinate system coincides with the centroid of τ.

To determine the order of accuracy of the proposed method we expand each value of ϕ at neighboring points in Taylor series about the centroid of τ, assuming sufficient smoothness in a neighborhood of the centroid. For example, $\bar{\phi}_I$ is given by

$$\bar{\phi}_I = \bar{\phi}_\tau + D_1 \bar{\phi}_\tau x_1^I + D_2 \bar{\phi}_\tau x_2^I + O(h^2), \tag{2.14}$$

where h is the grid parameter taken to be the greatest cell width of all control volumes, i.e.,

$$h = \max_{\tau\in\sigma}(4m_V(\tau)/m_S(\partial\tau)).$$

$m_S(\partial\tau)$ is the surface measure of the boundary of τ, $D_1\bar{\phi}_\tau$ is the derivative of $\bar{\phi}_\tau$ relative to its first argument and evaluated at the centroid of τ, and so on. Then, introducing such expressions in Eq. (2.10) and the latter in Eq. (2.7), and after a lengthy but straightforward manipulation (taking into account that $\Delta \neq 0$), we arrive at

$$\begin{aligned} R(x_1, x_2; \phi) &= \bar{\phi}_\tau + D_1\bar{\phi}_\tau x_1 + D_2\bar{\phi}_\tau x_2 + (aD_{1,1}\bar{\phi}_\tau + bD_{1,2}\bar{\phi}_\tau + cD_{2,2}\bar{\phi}_\tau)h^2 + o(h^2) \\ &= \phi(x_1, x_2) + O(h^2) \end{aligned} \tag{2.15}$$

for all $(x_1, x_2) \in \tau$, where $a, b, c \in \mathbf{R}$, and, for example, the coefficient of the mixed derivative, b, is given by

$$\begin{aligned} b = \big(&-C_1C_2^2D_yD_1^2 - C_1C_3^2D_yD_1^2 + C_1^2C_2D_yD_1D_2 + C_1C_2^2D_yD_1D_2 \\ &+ C_xC_1C_2D_1^2D_2 - C_xC_2^2D_1^2D_2 - C_1^2C_2D_yD_2^2 - C_2C_3^2D_yD_2^2 - C_xC_1^2D_1D_2^2 \\ &+ C_xC_1C_2D_1D_2^2 + C_1^2C_3D_yD_1D_3 + C_1C_3^2D_yD_1D_3 + C_xC_1C_3D_1^2D_3 \\ &- C_xC_3^2D_1^2D_3 + C_2^2C_3D_yD_2D_3 + C_2C_3^2D_yD_2D_3 + C_xC_2C_3D_2^2D_3 \\ &- C_xC_3^2D_2^2D_3 - C_1^2C_3D_yD_3^2 - C_2^2C_3D_yD_3^2 - C_xC_1^2D_1D_3^2 + C_xC_1C_3D_1D_3^2 \\ &- C_xC_2^2D_2D_3^2 + C_xC_2C_3D_2D_3^2\big)/\big(-C_2^2D_1^2 - C_3^2D_1^2 + 2C_1C_2D_1D_2 \\ &- C_1^2D_2^2 - C_3^2D_2^2 + 2C_1C_3D_1D_3 + 2C_2C_3D_2D_3 - C_1^2D_3^2 - C_2^2D_3^2\big), \end{aligned}$$

where

$$\begin{aligned} &C_1 = x_1^I/h, C_2 = x_1^{II}/h, C_3 = x_1^{III}/h, D_1 = x_2^I/h, \\ &D_2 = x_2^{II}/h, D_3 = x_3^{III}/h, C_x = x_1/h, D_y = x_2/h, \end{aligned}$$

and local smoothness of ϕ and

$$\bar{\phi}_\tau = \phi(x_1, x_2) + O(h^2), \qquad (x_1, x_2) \in \tau \tag{2.16}$$

were used.

In order to have an idea of the form and magnitude of the truncation errors in Eq. (2.15), we next consider the case of a regular grid composed of equilateral triangles. In this case, the first truncated terms are given by

$$R(x_1, x_2; \phi) = \phi(x_1, x_2) + \frac{h^2}{2}\left(-k_1D_{1,2}\bar{\phi}_\tau - \frac{k_2}{2}D_{1,1}\bar{\phi}_\tau + \frac{k_2}{2}D_{2,2}\bar{\phi}_\tau\right) + O(h^3), \tag{2.17}$$

where $x_1 = hk_1$, $x_2 = hk_2$, so that $k_1 \in [-1/2, 1/2]$ and $k_2 \in [-1, 1/2]$ within τ. To further investigate the nature of the error under this condition we perform a rotation of the coordinate system

$$\begin{bmatrix} x_1' \\ x_2' \end{bmatrix} = \begin{bmatrix} \cos\theta & \sin\theta \\ -\sin\theta & \cos\theta \end{bmatrix}\begin{bmatrix} x_1 \\ x_2 \end{bmatrix}, \tag{2.18}$$

which leads to

$$R(x_1', x_2'; \phi) = \phi(x_1', x_2') + \frac{h^2}{2}(AD_{1',1'}\bar{\phi}_\tau + BD_{1',2'}\bar{\phi}_\tau + CD_{2',2'}\bar{\phi}_\tau) + O(h^3), \quad (2.19)$$

where

$$A = -\frac{k_2}{2}\cos 2\theta - \frac{k_1}{2}\sin 2\theta, \qquad B = k_1 \cos 2\theta, \qquad C = \frac{k_2}{2}\cos 2\theta + \frac{k_1}{2}\sin 2\theta. \quad (2.20)$$

Hence, a rotation of 45° eliminates the mixed derivative, and we find

$$R(x_1', x_2'; \phi) = \phi(x_1', x_2') + \frac{k_1 h^2}{2}(-D_{1',1'}\bar{\phi}_\tau + D_{2',2'}\bar{\phi}_\tau) + O(h^3), \quad (2.21)$$

which shows that the leading term in the truncation error is compatible with a spatially propagating wave with constant unit speed.

Finally, the convective flux is evaluated at the control volume faces by solving a linear Riemann problem with right and left values given by the averaged values of R at right and left sides of the face, respectively. The convective velocity is given by the local value of the normal component of the velocity at the face.

Remark 2.1. In the case of the Navier–Stokes equations, the linear problem is substituted by the Riemann problem for the Burgers' equations in a local coordinate system with one of the coordinates aligned with the normal direction to the cell face. Namely, we choose the limit values of the reconstruction polynomials for the velocity components in x_1 and x_2 directions, which are upwinded with respect to the component of the velocity vector field (from the previous time step) normal to the cell face.

The left- and right-averaged value at the cell (control volume) face in the case of a triangle is just the value of R computed at the middle point of the cell face. So, C_i at a face $i \in \partial_\tau$ is approximated by

$$C_i \cong (\rho v_n m_S(i))_i \phi_i, \quad (2.22)$$

where ϕ_i is given by

$$\phi_i = \begin{cases} R(x_1(i-0), x_2(i-0); \phi), & \text{if } v_n > 0 \\ R(x_1(i+0), x_2(i+0); \phi), & \text{if } v_n < 0 \end{cases} \quad (2.23)$$

and $R(x_1(i \pm 0), x_2(i \pm 0); \phi)$ stands for the left limit $(i-0)$, or the right limit $(i+0)$ of R at the middle point of the cell face under consideration.

τ Is a Quadrilateral

In the case of a quadrilateral control volume, there is one more neighboring point available. Therefore, we use a bilinear reconstruction. Analogously to the triangle, we compute $a_1, a_2, a_3 \in \mathbf{R}$ that minimizes,

$$\chi(a_1, a_2, a_3) = \sum_{i \in i_\tau} \left(R\left(x_1^i, x_2^i; \bar{\phi}\right) - \bar{\phi}_i\right)^2, \quad (2.24)$$

with

$$R(x_1, x_2; \bar{\phi}) = \bar{\phi}_\tau + a_1 x_1 + a_2 x_2 + a_3 x_1 x_2. \quad (2.25)$$

It is easy to see that the solution of the latter problem is given by

$$\begin{bmatrix} \sum_{i\in i_\tau}\left(x_1^i\right)^2 & \sum_{i\in i_\tau}x_1^i x_2^i & \sum_{i\in i_\tau}\left(x_1^i\right)^2 x_2^i \\ \sum_{i\in i_\tau}x_1^i x_2^i & \sum_{i\in i_\tau}\left(x_2^i\right)^2 & \sum_{i\in i_\tau}x_1^i\left(x_2^i\right)^2 \\ \sum_{i\in i_\tau}\left(x_1^i\right)^2 x_2^i & \sum_{i\in i_\tau}x_1^i\left(x_2^i\right)^2 & \sum_{i\in i_\tau}\left(x_1^i\right)^2\left(x_2^i\right)^2 \end{bmatrix} \begin{bmatrix} a_1 \\ a_2 \\ a_3 \end{bmatrix} = \begin{bmatrix} \sum_{i\in i_\tau}(\bar{\phi}_i - \bar{\phi}_\tau)x_1^i \\ \sum_{i\in i_\tau}(\bar{\phi}_i - \bar{\phi}_\tau)x_2^i \\ \sum_{i\in i_\tau}(\bar{\phi}_i - \bar{\phi}_\tau)x_1^i x_2^i \end{bmatrix}. \tag{2.26}$$

The existence and the uniqueness of a solution of this linear system are assured if the matrix on the L.H.S. of Eq. (2.26) is non-degenerate. Let $g_{ij}, i, j = 1, 2, 3$, denote the components of this matrix. In order to characterize the set where the latter is degenerate, we first observe that g_{ij} can be written as

$$g_{ij} = v_i \cdot v_j, \tag{2.27}$$

where

$$v_1 = \left(x_1^i\right)_{i\in i_\tau}, \qquad v_2 = \left(x_2^i\right)_{i\in i_\tau}, \qquad \text{and} \qquad v_3 = \left(x_1^i x_2^i\right)_{i\in i_\tau}. \tag{2.28}$$

Hence, g_{ij} is analogous to a metric matrix in a three-dimensional subspace of $\mathbf{R}^4$, and it will be non-degenerate if and only if $\{v_1, v_2, v_3\}$ form a basis of this subspace. That is, it will be degenerate if and only if v_i is zero for some $i \in \{1, 2, 3\}$, or if there exist constants $a, b, c \in \mathbf{R}$, not all vanishing at the same time, such that

$$av_1 + bv_2 + cv_3 = 0. \tag{2.29}$$

Therefore, for $[g_{ij}]$ to be degenerate, either $v_3 = 0$ ($v_1, v_2 \neq 0$) or if $c \neq 0$, all neighboring points i_τ must lie over one and the same square hyperbola,

$$x_2 + \frac{a}{c} = \frac{b/c}{b/c + x_1}, \tag{2.30}$$

or, if $c = 0$, over the same line,

$$ax_1 + bx_2 = 0. \tag{2.31}$$

Since these curves have zero measure in $\mathbf{R}^2$, the probability of randomly generating such points is zero. However, the grid generation is not a random process and indeed there is a common situation where the neighboring points lead to $v_3 = 0$: for example, this happens when the grid is Cartesian. This result could have been anticipated by noticing that in such a case the curvature of the bilinear approximation is not "felt" by the minimization problem, and so an infinite number of coefficients would have resulted. In such cases, we fix the indeterminacy by taking the affine function as for a triangle control volume.

Consistency will not necessarily follow in an arbitrary coordinate system since, in general, the area inertia product, $I_{12} = \int_\tau x_1 x_2$, of the control volume does not vanish. This difficulty is overcome by rotating the local coordinate system to coincide with the principal axis of inertia of the control volume, where by definition $I_{12} = 0$. The rotation angle θ is given by

$$tg2\theta = \frac{2I_{12}}{I_{11} - I_{22}}, \tag{2.32}$$

where I_{11}, and I_{22} are the area moments of inertia in the x_1 and x_2 directions, respectively.

As for the triangle control volume, the convective flux is evaluated at the control volume faces by solving a linear Riemann problem with right and left values given by the averaged values of R at right and left sides of the face, respectively. Computations of the second moments and the limit mean values of R at a cell face are carried out by Gauss quadrature.

Finally, the order of the method is evaluated as in the triangle case by assuming sufficient smoothness of ϕ in a neighboring of the centroid, expanding in Taylor series the neighboring points to τ, and substituting in the reconstruction polynomial. Again, a lengthy but straightforward computation yields as leading truncation errors

$$\begin{aligned} R(x_1, x_2; \phi) &= \bar{\phi}_\tau + D_1\bar{\phi}_\tau x_1 + D_2\bar{\phi}_\tau x_2 + (\hat{a}D_{11}\bar{\phi}_\tau + \hat{e}D_{22}\bar{\phi}_\tau)h^2 + o(h^2) \\ &= \phi(x_1, x_2) + O(h^2), \end{aligned} \tag{2.33}$$

where $\hat{a}, \hat{e} \in \mathbf{R}$. Notice that in contrast to the triangle control volume, the mixed derivative does not appear. For example, in the case of a Cartesian grid with expanding/contracting ratios rat_1 and rat_2 in the x_1 and x_2 directions, respectively, we find

$$\hat{a} = C_x \frac{\left(\mathrm{rat}_1^3 - 1\right)}{2\left(1 + \mathrm{rat}_1^2\right)} \tag{2.34}$$

and

$$\hat{e} = C_y \frac{\left(\mathrm{rat}_2^3 - 1\right)}{2\left(1 + \mathrm{rat}_2^2\right)}. \tag{2.35}$$

Notice that for $\mathrm{rat}_1 = \mathrm{rat}_2 = 1$ the method is third-order accurate.

We have shown the method is consistent and second-order accurate. Here, it should be stressed that independently of its irregularity and composition, the method is second-order accurate in any grid topology. Indeed, a shape was never assumed for the neighbors, nor was any regularity assumed for the grid. This is in contrast to other methods for convection discretization commonly used in applications. These methods, the central differencing scheme, the minmod scheme, the MUSCL scheme [19], the linear upwind scheme, and the non-oscillatory UNO2 scheme [20] are only second-order accurate on uniform grids. This fact can be relevant in applications where almost invariably all grids are non-uniform and composed of a sensible (limited) number of points.

Diffusion Discretization Procedure

Diffusive fluxes are approximated as

$$D_i \equiv \int_i \overline{-\Gamma_\phi \frac{\partial \phi}{\partial n}} \approx -\Gamma_{\phi_{|i}} \frac{\partial \phi}{\partial n_{|i}} m_s(i), \qquad i \in \partial_\tau. \tag{2.36}$$

This approximation is accomplished by taking the central differencing of the interpolated adjacent node values, i.e.,

$$\frac{\partial \phi}{\partial n} \approx \frac{\phi^{n+} - \phi^{n-}}{\delta n}, \tag{2.37}$$

where ϕ^{n+} and ϕ^{n-} are linearly interpolated at the points indicated in Fig. 2.2, and δn is the distance in the normal direction between these points. The proposed approximation reverts

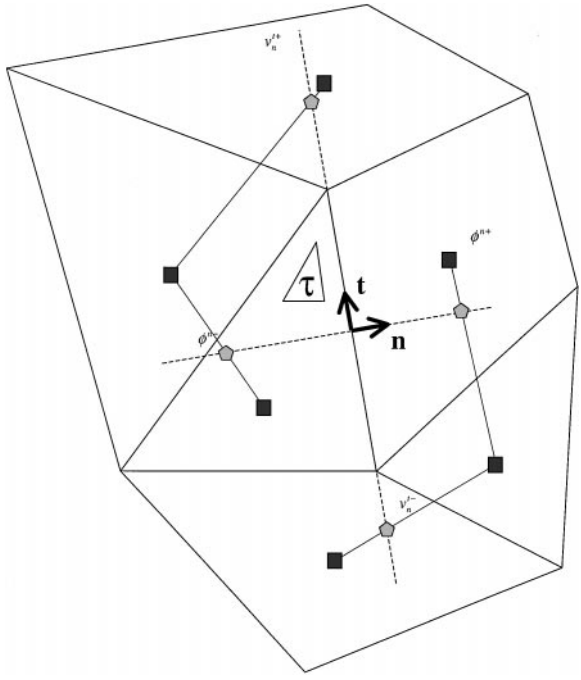

FIG. 2.2. Diffusion discretization.

to the second-order-accurate central differencing scheme in the case of a Cartesian grid. In general, it is exact for polynomials of first degree, i.e., affine functions.

Remark 2.2. In the case of the momentum (vector) equations, the diffusive flux, i.e., the deviatoric stress tensor, requires an extra interpolation in the direction tangent to the cell face. Indeed, given a face $i \in \partial\tau$ and its outward normal unit vector n, the deviatoric stress tensor σ_v, identified with a linear map when applied to n, gives the tension vector that acts at face i. Taking into account the Stokes model for σ_v, we obtain

$$\sigma_v(n) = \nu\left(2\frac{\partial v_n}{\partial n}n + \left(\frac{\partial v_n}{\partial t} + \frac{\partial v_t}{\partial n}\right)t\right), \tag{2.38}$$

where t is the tangent unit vector (see Fig. 2.2), $v_n = v \cdot n$ is the outward velocity component normal to face i, and $v_t = v \cdot t$ is the velocity component tangent to that face. So, in addition to the normal derivative, which is evaluated as indicated above, the computation of the term $\partial v_n/\partial t$ is required. This is carried out similarly to (2.37) as

$$\frac{\partial v_n}{\partial t} \approx \frac{v_n^{t+} - v_n^{t-}}{\delta t}, \tag{2.39}$$

where v_n^{t+}, v_n^{t-} are linearly interpolated at the points indicated in Fig. 2.2 and δt is analogous to δn.

Von Neumann Stability Analysis

For the sake of conciseness, we perform a von Neumann stability analysis for the case of the one-dimensional transport equation of a scalar ϕ. We assume a constant velocity u

(to the right) and a constant diffusive coefficient Γ_ϕ. The transport equation is discretized over a uniform mesh with grid parameter h and a constant time step Δt. We consider the discretization procedure for the diffusive flux as discussed above (which under the conditions of the present subsection reverts to the central differencing scheme) in the Euler implicit form and three temporal discretization procedures for the ULSS scheme, namely: (i) the Euler implicit approach, (ii) the Euler explicit approach, and (iii) the deferred-correction approach. The selected combinations cover the range of temporal discretization methods usually employed in the applications. At this point it should be emphasized that in the present paper we are only interested in computations for the steady state. So it is sufficient to consider methods that are only first order in time. In fact, at steady state, the numerical solution will be of the order of accuracy of the space discretization procedure, which in the present case is second-order.

Case I: Convection → implicit, diffusion → implicit. Under the conditions of the present subsection Eq. (2.3) simplifies to

$$\phi_i^{n+1} = \phi_i^n - \frac{\sigma_c}{4}\left(\phi_{i+1}^{n+1} + 3\phi_i^{n+1} - 5\phi_{i-1}^{n+1} + \phi_{i-2}^{n+1}\right) + \frac{\sigma_c}{\mathrm{Pe}_h}\left(\phi_{i+1}^{n+1} - 2\phi_i^{n+1} + \phi_{i-1}^{n+1}\right), \quad (2.40)$$

where $\sigma_c = \Delta t/\tau_c$ is the CFL number, with the convective time scale $\tau_c = h/u$, and $\mathrm{Pe}_h = uh/\Gamma_\phi$ is the grid Péclet number. Then, by substituting ϕ in Eq. (2.40) by its kth Fourier mode, i.e., $\phi \to \Phi \exp(ikx)$, where Φ is the amplification factor and k the wave number, and subsequently factoring the resulting equation, we obtain the following expression for the amplification factor,

$$\Phi = \frac{4}{4 + 8\sigma_c/\mathrm{Pe}_h(1-\cos\beta) + \sigma_c(\exp(-2i\beta) - 5\exp(-i\beta) + 3 + \exp(i\beta))}, \quad (2.41)$$

where $\beta = kh$. The method is von Neumann stable if $|\Phi| \le 1$. So, the implicit method is unconditionally stable. In fact, it is sufficient to observe that the denominator of Eq. (2.41) can be written as

$$|\Phi|_{\mathrm{den}} = \sqrt{\left(4 + 8\frac{\sigma_c}{\mathrm{Pe}_h}(1-\cos\beta) + \sigma_c(1-\cos\beta)^2\right)^2 + \sigma_c^2(6\sin\beta - \sin 2\beta)^2}, \quad (2.42)$$

which is greater than 4.

Case II: Convection → explicit, diffusion → implicit. With the same notation as above, the discretized equation now reads

$$\phi_i^{n+1} = \phi_i^n - \frac{\sigma_c}{4}\left(\phi_{i+1}^{n} + 3\phi_i^{n} - 5\phi_{i-1}^{n} + \phi_{i-2}^{n}\right) + \frac{\sigma_c}{\mathrm{Pe}_h}\left(\phi_{i+1}^{n+1} - 2\phi_i^{n+1} + \phi_{i-1}^{n+1}\right) \quad (2.43)$$

and the corresponding amplification factor is given by

$$\Phi = \frac{\mathrm{Pe}_h \exp(-2i\pi\eta)(-4\exp(4i\pi\eta) + \sigma_c(1 - 5\exp(2i\pi\eta) + 3\exp(4i\pi\eta) + \exp(6i\pi\eta)))}{4(\sigma_c(1 - 2\exp(2i\pi\eta) + \exp(4i\pi\eta)) - \exp(2i\pi\eta)\mathrm{Pe}_h)}, \quad (2.44)$$

where $\eta = \frac{h}{\lambda}$, and λ is the wavelength, $\lambda = \frac{2\pi}{k}$. So, η is the reciprocal of the non-dimensional wavelength. Contrary to the previous case, the present combination is not unconditionally stable. In fact, to be von Neumann stable it is necessary that $\eta = 0$, where $|\Phi| = 1$, be a point of maximum. That is, Pe_h and σ_c must satisfy

$$\left.\frac{\partial^2 |\Phi|}{\partial \eta^2}\right|_{\eta=0} \leq 0,$$

or

$$4\pi^2 \left(\left((\sigma_c - 2)^2 - 4(1-\sigma_c)\right) - \frac{\left(\mathrm{Pe}_h^2 - (2\sigma_c + \mathrm{Pe}_h)\right)}{\mathrm{Pe}_h^2} \right) \leq 0. \tag{2.45}$$

So, it is necessary that

$$\sigma_c \mathrm{Pe}_h \leq 2. \tag{2.46}$$

This last condition is also sufficient. In fact, by taking the derivative of $|\Phi|$ with respect to η and then substituting σ_c by $2/\mathrm{Pe}_h$ yields

$$\begin{aligned} &\frac{\partial |\Phi|}{\partial \eta}_{|(2/\mathrm{Pe}_h, \mathrm{Pe}_h, \eta)} \\ &= \frac{8\pi \mathrm{Pe}_h^2 \cos(\pi\eta)\left(22 - \mathrm{Pe}_h^2 + \mathrm{Pe}_h^3 - 8\cos(2\pi\eta) - 3\mathrm{Pe}_h^2 \cos(2\pi\eta) + 2\cos(2\pi\eta)\sin^3(\pi\eta)\right)}{\left(4\cos(2\pi\eta) - 4 - \mathrm{Pe}_h^2\right)^3 \left|\Phi\left(\frac{2}{\mathrm{Pe}_h}, \mathrm{Pe}_h, \eta\right)\right|}. \end{aligned} \tag{2.47}$$

This result follows from noticing that $|\Phi|$ is periodic with respect to η with unit period, that it is even with respect to $\eta^{-1/2}$, and that

$$\frac{\partial |\Phi|}{\partial \eta}_{|(2/\mathrm{Pe}_h, \mathrm{Pe}_h, \eta)} \leq 0, \tag{2.48}$$

for all $\eta \in [0, 1/2]$. In conclusion, the ULSS for the explicit–implicit case is stable if and only if $\sigma_c \mathrm{Pe}_h \leq 2$.

Case III: Convection → deferred-correction, diffusion → implicit. In this case, the discretized equation reads

$$\begin{aligned} \phi_i^{n+1} = \phi_i^n &- \frac{\sigma_c}{4}\left(\phi_i^{n+1} - \phi_{i-1}^{n+1}\right) - \frac{\sigma_c}{4}\left(\phi_{i+1}^n + 2\phi_i^n - 4\phi_{i-1}^n + \phi_{i-2}^n\right) \\ &+ \frac{\sigma_c}{\mathrm{Pe}_h}\left(\phi_{i+1}^{n+1} - 2\phi_i^{n+1} + \phi_{i-1}^{n+1}\right), \end{aligned} \tag{2.49}$$

to which corresponds an amplification factor of

$$\Phi = \frac{\mathrm{Pe}_h \exp(-2i\pi\eta)(4\exp(4i\pi\eta) + \sigma_c(-1 + 4\exp(2i\pi\eta) - 2\exp(4i\pi\eta) - \exp(6i\pi\eta)))}{\sigma_c(-4 + 8\exp(2i\pi\eta) - 4\exp(4i\pi\eta)) + 4\mathrm{Pe}_h \exp(4i\pi\eta) + \sigma_c \mathrm{Pe}_h(\exp(2i\pi\eta) - 1)}. \tag{2.50}$$

An analysis analogous to the previous one shows that the ULSS for the deferred-correction–implicit combination is stable if and only if $\sigma_c \mathrm{Pe}_h \leq 4$.

In the literature it is frequently claimed that deferred correction can stabilize the convergence procedure (see, for example [21–23]). However, as this relation indicates under the present conditions the stability gain is only marginal for high Pe_h.

Boundary Conditions

We consider two types of boundary conditions: (i) Dirichlet and (ii) von Neumann.

Dirichlet boundary condition. When the value of the variable ϕ is known at a boundary $\partial\tau_B$, we use it directly in the convective flux, i.e.,

$$C_B = \rho_B (v_n)_B \phi_B m_S(\partial\tau_B), \tag{2.51}$$

where the subscript B denotes the corresponding value at the boundary $\partial\tau_B$. On the other hand, for the diffusive flux we compute the (exterior) normal derivative as

$$\frac{\partial\phi}{\partial n_{|B}} = -\left(\frac{1}{(\delta n)_I} + \frac{1}{(\delta n)_{II}}\right)\phi_B + \frac{(\delta n)_{II}}{(\delta n)_I}\frac{1}{(\delta n)_{II} - (\delta n)_I}\phi_I + \frac{(\delta n)_I}{(\delta n)_{II}}\frac{1}{(\delta n)_I - (\delta n)_{II}}\phi_{II}, \tag{2.52}$$

where the notation is defined in Fig. 2.3. This method corresponds to an immediate generalization of the one-sided second-order method for approximating a derivative.

Von Neumann boundary condition. In contrast with the previous case, it is the derivative $\frac{\partial\phi}{\partial n}$ that is known at a boundary $\partial\tau_B$. So, for the diffusive flux we compute

$$D_B = -(\Gamma_\phi)_B \frac{\partial\phi}{\partial n_{|B}} m_S(\partial\tau_B). \tag{2.53}$$

Finally, for a control volume adjacent to the boundary $\partial\tau_B$, we use $\partial\phi/\partial n_{|B}$ in the reconstruction. This is attained by modifying the unrestrained minimization problem into a conditioned one. For instance, in the case of a triangular control volume we solve the

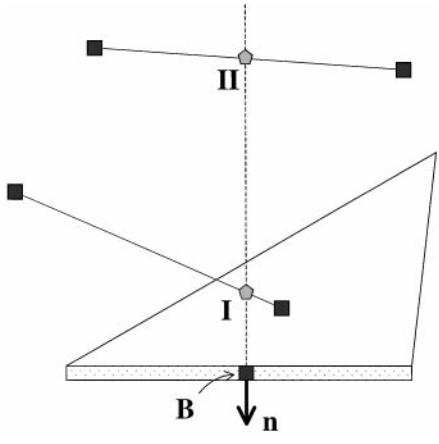

FIG. 2.3. Diffusion discretization at boundaries.

following: find a_1, a_2 such that

$$\chi(a_1, a_2) = \sum_{i \in i_\tau} \left(R\left(x_1^i, x_2^i; \phi\right) - \bar{\phi}_i\right)^2 = \sum_{i \in i_\tau} \left(\bar{\phi}_\tau + a_1 x_1^i + a_2 x_2^i - \bar{\phi}_i\right)^2 \quad (2.54)$$

is minimum and

$$\frac{\partial R}{\partial n_{|B}} = \frac{\partial \phi}{\partial n_{|B}}. \quad (2.55)$$

This problem can easily be solved using the Lagrange multiplier method; that is, we solve, for $(a_1, a_2, \upsilon) \in \mathbf{R}^3$, the equations

$$\begin{aligned} \nabla\chi(a_1, a_2) &= \upsilon \nabla\gamma(a_1, a_2) \\ \gamma(a_1, a_2) &\equiv a_1 n_1 + a_2 n_2 = 0, \end{aligned} \quad (2.56)$$

where υ is the Lagrange multiplier. The quadrilateral control volume is treated analogously.

In Section 4, we study the influence of the boundary conditions on the quality of the results.

3. FRACTIONAL STEP PROJECTION METHOD—FraSp

Having established the discretized version of the convection–diffusion equation, we proceed with the derivation of the projection method for the computation of incompressible fluid flow on unstructured hybrid meshes.

Given a grid σ, we define the dual grid σ^* by joining the centroids of control volumes concurrent to the vertices (see Fig. 3.1). Let V denote the linear space of vector fields with

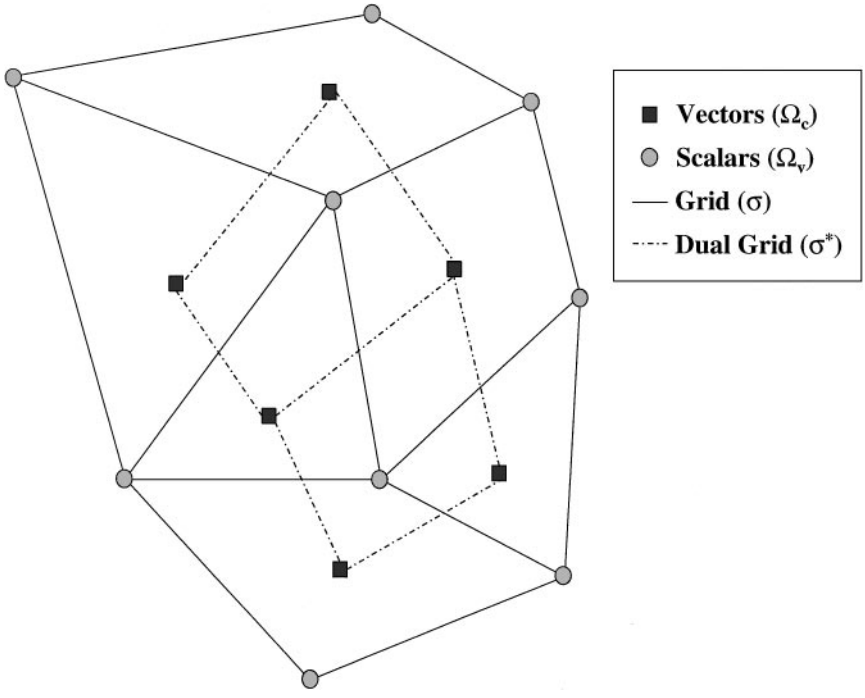

FIG. 3.1. Mesh arrangement.

support at the centroid of the mesh control volumes, i.e.,

$$V = \{u \in \mathsf{X}(\Omega) : u_i = 0, i \notin \Omega_c\}, \tag{3.1}$$

where

$$u \in \mathsf{X}(\Omega) \Leftrightarrow u : \Omega \to \Omega \times \mathbf{R}^d,$$

with $u(i) = (i, u_i)$, $i \in \Omega$, $u_i \in \mathbf{R}^d$ and where Ω_c stands for the set of centroids of the mesh control volumes, and $\dim V = N$. Similarly, let S be the linear space of scalar fields with support at the vertices of the mesh control volumes, i.e.,

$$S = \{\phi \in \mathsf{F}(\Omega) : \phi_i = 0, i \notin \Omega_v\}, \tag{3.2}$$

where

$$\phi \in \mathsf{F}(\Omega) \Leftrightarrow \phi : \Omega \to \Omega \times \mathbf{R},$$

with $\phi(i) = (i, \phi_i)$, $i \in \Omega$, $\phi_i \in \mathbf{R}$ and where Ω_v stands for the set of vertices of the mesh control volumes, and $\dim S = M$. Define the inner product over V as

$$\begin{aligned} (\cdot, \cdot)_V : V \times V &\to \mathbf{R} \\ :(u, v) &\mapsto (u, v)_V \equiv \sum_{i \in \Omega_c} u_i \cdot v_i m_V(\tau(i)), \end{aligned} \tag{3.3}$$

where m_V is the Lebesgue measure and $\tau(i)$ is the control volume associated with centroid i, $i \in \Omega_c$. Let

$$\begin{aligned} (\cdot, \cdot)_S : S \times S &\to \mathbf{R} \\ :(\varphi, \psi) &\mapsto (\varphi, \psi)_S \equiv \sum_{i \in \Omega_v} \varphi_i \psi_i m_V(\tau^*(i)) \end{aligned} \tag{3.4}$$

be the inner product over S, where $\tau^*(i)$ is the control volume associated with the vertices i, $i \in \Omega_v$. With the above definitions $(V, (\cdot, \cdot)_V)$ and $(S, (\cdot, \cdot)_S)$ are Hilbert spaces. In fact, the defined inner products are the pull back through a "weighted coordinate isomorphism" to $\mathbf{R}^N$ and $\mathbf{R}^M$, respectively, of the standard dot product.

We consider the sections $e : \Omega_c \to \Omega_c \times \mathbf{E}(\mathbf{R}^d)$, and $\xi : \Omega_v \to \Omega_v \times \mathbf{E}(\mathbf{R})$ of the trivial fiber bundles $(\Omega_c \times \mathbf{E}(\mathbf{R}^d), pr_1, \Omega_c)$ and $(\Omega_v \times \mathbf{E}(\mathbf{R}), pr_1, \Omega_v)$, respectively, given by

$$e(i) = (i, (e_1, \ldots, e_d)), \qquad \xi(j) = (j, 1) \tag{3.5}$$

for all $i \in \Omega_c$, $j \in \Omega_v$, where $\{e_1, \ldots, e_d\}$ is the canonical basis of $\mathbf{R}^d$. For instance, $\mathbf{E}(\mathbf{R}^d)$ is the subspace of the Cartesian product

$$\underbrace{\mathbf{R}^d \times \cdots \times \mathbf{R}^d}_{d \text{ times}}$$

composed of points $p = (p_1, \ldots, p_d)$ such that all components $p_1, \ldots, p_d \in \mathbf{R}^d$ constitute a basis of $\mathbf{R}^d$, and $pr_1 : \Omega_c \times \mathbf{E}(\mathbf{R}^d) \to \Omega_c$ is the projection on the first factor. Similarly, we define $(\Omega_v \times \mathbf{E}(\mathbf{R}), pr_1, \Omega_v)$ (notice that we use $pr_1 : \Omega_v \times \mathbf{E}(\mathbf{R}) \to \Omega_v$ for this fiber bundle as well).

Over these spaces, we then define the gradient operator $G: S \to V$ as

$$G\phi = \sum_{i \in \Omega_c} \sum_{j=1}^{d} (G\phi)_j(i) e_j(i) \tag{3.6}$$

for all $\phi \in S$, where

$$(G\phi)_j(i) \equiv \frac{1}{m_V(\tau(i))} \sum_{f \in \partial\tau(i)} \phi_f m_S(f) n_j(f) \in \mathbf{R} \tag{3.7}$$

for all $i \in \Omega_c$ and $j = 1, \ldots, d$, where $\tau(i)$ is the control volume associated with the centroid i, $\partial\tau(i)$ denotes its boundary, i.e., $\partial\tau(i) = \{f_1, \ldots, f_{\#f(i)}\}$, $\#f(i)$ is the number of cell faces associated with the control volume $\tau(i)$, $i \in \Omega_c$, ϕ_f is the arithmetic mean of the values of the function ϕ at the vertices associated with the cell face f, and $n_j(f)$ is jth component of the unit exterior normal vector at cell face f, $j = 1, \ldots, d$. We similarly define the divergence operator $D: V \to S$ as

$$Du = \sum_{i \in \Omega_v} Du(i) \xi(i) \tag{3.8}$$

for all $u \in V$, where

$$Du(i) \equiv \frac{1}{m_V(\tau^*(i))} \sum_{f \in \partial\tau^*(i)} u_f \cdot n_f m_S(f) \in \mathbf{R} \tag{3.9}$$

for all $i \in \Omega_v$, where $\tau^*(i)$ stands for the dual control volume associated with the vertices i, $\partial\tau^*(i)$ denotes its boundary, i.e., $\partial\tau^*(i) = \{f_1, \ldots, f_{\#f(i)}\}$, $\#f(i)$ is the number of cell faces associated with the control volume $\tau^*(i)$, $i \in \Omega_v$, u_f is the arithmetic mean of the vector field u at the vertices associated with the cell face f, and n_f is the unit exterior normal vector at cell face f.

With the above definitions for the projection method, we proceed with a fractional time evolution given by the solution of the following linear problem FS: Find $u^{n+1,0} \in V$ such that

$$\frac{u^{n+1,0} - u^n}{\Delta t} + \mathsf{D}\big(Mu^n \otimes Cu^{n+1,0} - \sigma_v(u^{n+1,0})\big) = -Gp^n \qquad \text{and} \qquad u|_{\partial\Omega_c}^{n+1,0} = g_{t^{n+1}}, \tag{3.10}$$

where $g_t: \partial\Omega \to \partial\Omega \times \mathbf{R}^d$ at each time t is a given vector field over the domain boundary $\partial\Omega$, $\partial\Omega_c$ is the set of points on $\partial\Omega$ at the center of the edges of the control volumes which are adjacent to the boundaries, u is the velocity vector field, p is the pressure field, Δt is the time step, σ_v is the deviatoric stress tensor, $\otimes$ denotes the tensor product, and the superscript n denotes the value at the nth time step. In this expression, $\mathsf{D}: V_e \otimes V_e \to V$, where V_e stands for the linear space of discrete vector fields with support at the control volume edges, is the divergence operator for tensor fields defined similarly to the divergence operator for the convection-diffusion equation, with the mass flux computed with the velocity vector field at the nth time step.

The existence and uniqueness of a solution to problem FS follow at once from

$$\mathsf{E}(u^n)u^{n+1,0} = \frac{1}{\Delta t}\big(id_V + \Delta t \mathsf{D}\big(Mu^n \otimes C \cdot - \sigma_V(\cdot)\big)\big)u^{n+1,0} = \frac{u^n}{\Delta t} - Gp^n,$$

which means that for small Δt,

$$\Delta t \left\| \mathsf{D}\left(M u^n \otimes C \cdot -\sigma_V(\cdot) \right) \right\| < 1,$$

which in turn implies that $\mathsf{E}(u^n)$ has an inverse in the Banach algebra of linear operators over V.

The influence of the CFL number on the convergence rate is investigated in Section 4.

We complete the time evolution first with the projection of the resulting velocity vector field $u^{n+1,0}$ into the space of solenoidal vector fields

$$u^{n+1} = P_o\left(u^{n+1,0} - v_d\right) + v_d, \tag{3.11}$$

where $v_d \in \ker D \wedge v_d(i) = g_t(i)$, $i \in \partial\Omega$, and where the orthogonal projection operator $P_o: V_o \to \ker D_o$ is defined as

$$P_o u = u_d$$

for all $u \in V_o$, with

$$u = u_d + D_o^* \phi, \qquad u_d \in \ker D_o, \qquad \phi \in S, \tag{3.12}$$

where we have used the Hodge decomposition of $V_o = \ker D_o \oplus \operatorname{im} D_o^*$, with $D_o^*: S \to V_o$ being the adjoint operator of the restricted divergence operator $D_o: V_o \to S$, $D_o \equiv D_{|V_o}$. In these expressions, V_o stands for the subspace of V consisting of the vector fields vanishing at the domain boundary. We then compute the pressure field from a second fractional step:

$$\frac{u^{n+1} - u^n}{\Delta t} + \mathsf{D}\left(M u^n \otimes C u^{n+1,0} - \sigma_v(u^{n+1,0}) \right) = -G p^{n+1}. \tag{3.13}$$

Remark 3.1. The projection into the space of solenoidal vector fields could have been performed by straightforward application of the orthogonal projection $P: V \to \ker D$; however, the resulting vector field would not, in general, satisfy the prescribed boundary conditions. The proposed strategy circumvents this problem using the projection operator P_o. To this end, a vector field vanishing at the domain boundary is needed. This can be attained by subtracting from $u^{n+1,0}$ a vector field that is equal to zero at the interior of the domain and equal to the prescribed boundary conditions at the boundary; however, the resulting vector field u^{n+1} would not, in general, be solenoidal. Thus, the need for a solenoidal vector field v_d is shown.

Remark 3.2. There are several different but equivalent procedures for implementing the projection operator. We next consider three of them, namely: (a) the Galerkin approach, (b) the Variational approach, and (c) the Chorin approach. In the Galerkin approach, we first determine a basis of $\ker D_0$, say $\bar{e} = \{\bar{e}_a\}_{a=1,\ldots,\dim \ker D_0}$. This can be accomplished, for instance, by considering the Hodge decomposition which asserts that $\ker D_0 = (\operatorname{im} D_0^*)^\perp$. Therefore, a basis for $\ker D_0$ can be obtained by considering the images through $(D_0^*)^\perp_{|\tau} \phi \equiv ([(D_0^*)_{|\tau}\phi]_2, -[(D_0^*)_{|\tau}\phi]_1)$ of a basis of S. Finally, the computation of the projection $P_0 v = w \in \ker D_0$ of any vector field $v \in V_0$ is effected by solving the following linear system of equations: $\sum_{i=1}^N A_a^i w_i = \bar{v}_a$, $a = 1, \ldots, N$, where $\bar{v}_a = (v, \bar{e}_a)_V$

is the ath covariant component of $v \in V_0$ in the basis $\bar{e}$, $a = 1, \ldots,$ dim ker D_0 (we refer to $\bar{e}$ as a basis of V_0; this should be understood in the sense of an extension of $\bar{e}$ to a basis of V_0, which, of course, always exists), A_a^i is the (i, a) entry in change of basis matrix $\bar{e}_a = \sum_{i=1}^{N} A_a^i \hat{e}_i$, $a = 1, \ldots, N$, $w_i = (w, \hat{e}_i)$ is the ith covariant component of w in the working basis $\{\hat{e}_i\}_{i=1,\ldots,N}$, and $i = 1, \ldots, N$. One such procedure has been successfully implemented in the framework of a Cartesian grid by Bell *et al.* [11].

In the variational approach, we can use the fact that for a given $v \in V_0$, $P_0 v = w \in \ker D_0$ is *the* solution of the following minimal problem VA: Find $w \in \ker D_0$ such that

$$\|v - w\| = \min!.$$

The solution of VA can be easily obtained from the Lagrange multipliers method if we recall that these multipliers are nothing but the components of the gradient of the function we want to minimize (in the present case, $f(w) = \|v - w\|$) in the space normal to the restriction manifold (in the present case, ker D_0). So, by using the Hodge decomposition, the solution of VA is computed by solving the linear problem

$$\begin{bmatrix} D_0 & 0 \\ \mathrm{id}_V & D_0^* \end{bmatrix} \begin{bmatrix} w \\ \phi \end{bmatrix} = \begin{bmatrix} 0 \\ v \end{bmatrix}, \tag{3.14}$$

where $\mathrm{id}_V : V \to V$ is the identity operator, and $\phi \in S$ is the function corresponding to the Lagrange multipliers.

Finally, in the Chorin approach, for a given $v \in V_0$, $P_0 v = w \in \ker D_0$ can be determined by subtracting from $v \in V_0$ its orthogonal complement. The latter, by the Hodge decomposition, is to be found in im D_0^*.

Under favorable conditions, the Galerkin approach can result in a smaller system of equations. However, due to non-local basis elements, for multiply connected regions, the matrix for the Galerkin procedure is more complex (see, for example, [11, 12]). Combination of the first and second block lines in Eq. (3.14) of the variational procedure using the Lagrange multipliers leads to the Chorin approach. Other minimizing techniques for the variational approach could be used. However, to the authors' knowledge, so far they have not been considered in the literature. The minimization property of the projection method also implies that the "perturbation" in the velocity field introduced in the projection step is the smallest necessary variation to change this field into a solenoidal one. In the present work, the decomposition will be carried out via the direct determination of the orthogonal component, i.e., the Chorin approach.

Remark 3.3. Using the Chorin approach, we can skip the actual computation of v_d noticing that from Eq. (3.12) we have

$$P_o\left(u^{n+1,0} - v_d\right) = u^{n+1,0} - v_d - D_o^* \phi.$$

Nevertheless, the existence of v_d is required and can be easily obtained for some function $\phi \in S$. So,

$$u^{n+1} = P_o\left(u^{n+1,0} - v_d\right) + v_d = u^{n+1,0} - D_o^* \phi. \tag{3.15}$$

The function $\phi \in S$ can be determined as follows. Since $u^{n+1} \in \ker D$, it follows that $(Du^{n+1}, \psi)_S = 0$, for all $\psi \in S$. Substitution of Eq. (3.15) for u^{n+1} yields

$$(Du^{n+1,0}, \psi)_S = (DD_o^*\phi, \psi)_S = (D_o^*\phi, D_o^*\psi)_V \tag{3.16}$$

for all $\psi \in S$. In particular, for

$$i \in \Omega_v \colon \psi_i(j) \equiv \begin{cases} (j,1), & \text{if } j \in \Omega_v \wedge j = i \\ (j,0), & \text{if } j \in \Omega_v \wedge j \neq i \end{cases}, \tag{3.17}$$

we get the linear system of equations

$$\sum_{i \in \Omega_v} \phi^i (D_o^*\psi_i, D_o^*\psi_j)_V = \left(Du^{n+1,0}, \psi_j\right)_S, \qquad j \in \Omega_v, \tag{3.18}$$

where $\phi = \sum_{i \in \Omega_v} \phi^i \psi_i$. Solving this system of equations yields $\phi \in S$.

Remark 3.4. The convergence of Eq. (3.13) provides a solution $[p] \in S/\ker G$. Let

$$\begin{aligned} \hat{G} \colon S/\ker G &\to V \\ :[p] &\mapsto \hat{G}[p] \equiv Gp, \end{aligned} \tag{3.19}$$

which is clearly well defined. Then,

$$\operatorname{im} \hat{G} = \operatorname{im} G. \tag{3.20}$$

In other words, even though the value of pressure can be indeterminate, its gradient is well defined and satisfies (3.13). In fact, consider the case where the control volume τ is a triangle. Then, locally, the gradient operator is given by

$$Gp_{|\tau} = \frac{1}{m_V(\tau)} \begin{bmatrix} \frac{(p_I + p_{II})}{2} A^x_{I,II} + \frac{(p_{II} + p_{III})}{2} A^x_{II,III} + \frac{(p_{III} + p_I)}{2} A^x_{III,I} \\ \frac{(p_I + p_{II})}{2} A^y_{I,II} + \frac{(p_{II} + p_{III})}{2} A^y_{II,III} + \frac{(p_{III} + p_I)}{2} A^y_{III,I} \end{bmatrix}_\tau, \tag{3.21}$$

where p is the pressure and A stands for the (externally) oriented vector areas at vertices *I*, *II*, and *III* and the corresponding edges, respectively (see Fig. 3.2). Hence, $\ker G$ is given

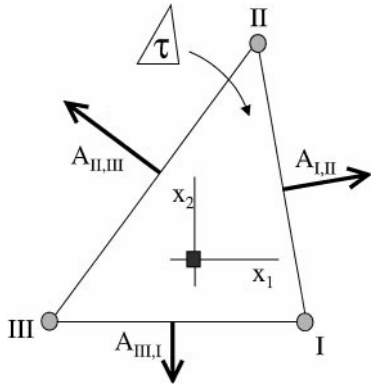

FIG. 3.2. Notation for local gradient computation.

by

$$Gp_{|\tau} = \frac{1}{m_V(\tau)} \begin{bmatrix} \frac{(p_I + p_{II})}{2} A^1_{I,II} + \frac{(p_{II} + p_{III})}{2} A^1_{II,III} + \frac{(p_{III} + p_I)}{2} A^1_{III,I} \\ \frac{(p_I + p_{II})}{2} A^2_{I,II} + \frac{(p_{II} + p_{III})}{2} A^2_{II,III} + \frac{(p_{III} + p_I)}{2} A^2_{III,I} \end{bmatrix}_\tau = 0 \qquad (3.22)$$

for all $\tau \in \sigma$. Equation (3.22) can then be written as

$$\begin{bmatrix} A^1_{I,II} + A^1_{III,I} & A^1_{I,II} + A^1_{II,III} \\ A^2_{I,II} + A^2_{III,I} & A^2_{I,II} + A^2_{II,III} \end{bmatrix} \begin{bmatrix} p_I \\ p_{II} \end{bmatrix} = - \begin{bmatrix} \left(A^1_{II,III} + A^1_{I,III}\right) p_{III} \\ \left(A^2_{II,III} + A^2_{I,III}\right) p_{III} \end{bmatrix}. \qquad (3.23)$$

From

$$A_{I,II} + A_{II,III} + A_{III,I} = 0 \qquad (3.24)$$

it follows that

$$\det \begin{bmatrix} A^1_{I,II} + A^1_{III,I} & A^1_{I,II} + A^1_{II,III} \\ A^2_{I,II} + A^2_{III,I} & A^2_{I,II} + A^2_{II,III} \end{bmatrix} = A_{II,III} \times A_{III,I}. \qquad (3.25)$$

Since τ is a non-degenerate triangle we obtain

$$p_I = p_{II} = p_{III}. \qquad (3.26)$$

So, for a grid consisting of triangles, $\dim \ker G = 1$, and as it happens with the continuum case, only constant functions have zero gradient. A similar (but lengthier) computation shows that in the case of a quadrilateral the local condition is

$$p_I = p_{III} \qquad \text{and} \qquad p_{II} = p_{IV},$$

where vertices *I* and *III*, and *II* and *IV* are opposite vertices, corresponding to the so-called checkerboard mode [7]. Hence, for a grid consisting only of quadrilaterals, we have $\dim \ker G = 2$.

Therefore, we only use the intermediate pressure values for the computation of the pressure gradient (it is necessary, in the momentum equation, for the pressure gradient to be the gradient of a function). The actual value of the pressure, when it is required, is evaluated by the reconstruction of the pressure field from the pressure gradient. To this end, we triangulate the dual grid and interpolate each component of the pressure gradient over this new grid, by use of the linear finite element interpolation. In this way, each component of the gradient is continuous. Hence, pressure is C^1 and can be recovered by: (i) fixing the value of the pressure at one point, (ii) integrating over each edge using the formula

$$p_1 = p_0 + \int t \cdot \operatorname{grad} p \, ds, \qquad (3.27)$$

where p_0, p_1 are endpoints in an edge, t is the unit vector in the edge pointing from p_0 to p_1, and ds is its arc length.

Remark 3.5. We solve the momentum equations for u_1 and u_2 simultaneously, using the ILU-preconditioned BI-CGSTAB [24]. Because of the symmetry and positivity of the matrix, we use the ILU-preconditioned conjugate gradient (PCG) method in the projection step.

Remark 3.6. Computation of pressure in the second fractional step can be simplified by: (i) subtracting Eq. (3.10) from Eq. (3.13), yielding

$$Gp^{n+1} = Gp^n + \frac{1}{\Delta t} D_0^* \phi,$$

where we have used Eq. (3.15); and (ii) approximating $D_0^* \approx -G_0$ (notice that for a uniform Cartesian grid, $G_0 = -D_0^*$, and in general, $D_{0|\tau}^* \phi = -G_{0|\tau}\phi + O(h)$).

Hence, writing

$$p^{n+1} = p^n - \frac{\phi}{\Delta t},$$

we obtain the correct solution for the momentum equation as long as the overall method converges to a steady state, and $\phi \in \ker G_0 \cap \ker D_0^*$. This last condition is met in hybrid grids for which $\dim \ker D_0^* = 1$. This is the case of hybrid grids with triangles. Indeed, for a triangle control volume τ, we have (see Fig. 3.3 for notation definition)

$$D_0^* \phi_{|\tau} = \frac{1}{m_V(\tau)} \begin{bmatrix} \frac{\tilde{A}^1_{I,II}}{2}(\phi_I - \phi_{II}) + \frac{\tilde{A}^1_{II,III}}{2}(\phi_{II} - \phi_{III}) + \frac{\tilde{A}^1_{III,I}}{2}(\phi_{III} - \phi_I) \\ \frac{\tilde{A}^2_{I,II}}{2}(\phi_I - \phi_{II}) + \frac{\tilde{A}^2_{II,III}}{2}(\phi_{II} - \phi_{III}) + \frac{\tilde{A}^2_{III,I}}{2}(\phi_{III} - \phi_I) \end{bmatrix}$$

and the result follows similarly as in the case of the gradient (compare with Remark 3.4).

On the other hand, if the grid is composed only of quadrilaterals we can, for instance, fix the value of ϕ at one grid point. Alternatively, we let the PCG method find $\phi \in \ker D_0^*$.

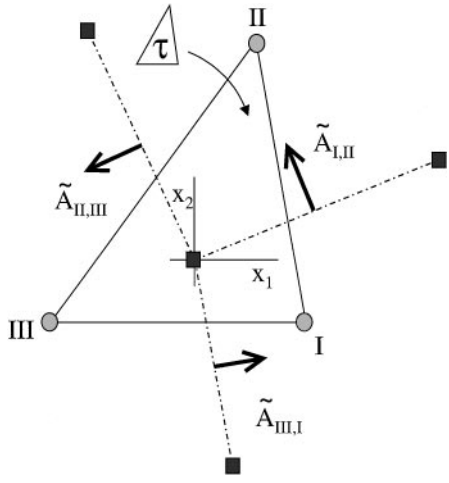

FIG. 3.3. Notation for local gradient (skew adjoint of the divergence operator) computation.

In Section 4, we study the possibility of using a factor α_p in the update of the pressure field, i.e.,

$$p^{n+1} = p^n - \alpha_p \frac{\phi}{\Delta t}. \tag{3.28}$$

Remark 3.7. In the literature, it is mentioned that a second projection step can be advantageous, at least in conjunction with a pressure correction strategy [25]. In the framework of the projection methods, the pressure correction schemes can be regarded as projection methods with an oblique projection. This is in contrast with the orthogonal projection used in the present work. Numerical experiments carried out by the authors, using a second projection, displayed only a marginal gain in the number of iterations necessary for convergence (of the order of 3%), while highly penalizing the CPU time. This suggests that a second projection step is not necessary in the present method.

At this point it is useful to sum up the steps in a workable algorithm. Starting with (u^0, p^0), we first compute the coefficients and pressure gradient in the discretized Navier–Stokes equations, using u^n and p^n. Then, we solve Eq. (3.10) for $u^{n+1,0}$. Next, we apply the projection to the intermediate discrete vector field $u^{n+1,0}$ by computing ϕ from Eq. (3.18), yielding u^{n+1}. Finally, we update pressure using Eq. (3.28). We proceed with these steps until the steady state is achieved. This is established when

$$\mathrm{Max}\left(\|Du^{n+1,0}\|_\infty \frac{\ell_{\mathrm{ref}}}{u_{\mathrm{ref}}}, \left\| \frac{u^{n+1,0} - u^n}{\Delta t} \right\|_\infty \frac{\ell_{\mathrm{ref}}}{u_{\mathrm{ref}}^2} \right) < \varepsilon,$$

where ε is a given convergence level (typically $\varepsilon = 10^{-6}$), and ℓ_{ref} and u_{ref} are reference length and speed, respectively.

4. NUMERICAL RESULTS

This section presents numerical calculations for four test cases of different complexity aiming to assess the accuracy, robustness, and efficiency of the proposed method. These test cases include: (a) the two-dimensional convection–diffusion transport of a scalar, (b) the incompressible viscous flow through a convergent channel, (c) the lid cavity flow with body forces, and (d) the lid cavity flow.

Transport of a Passive Scalar

We consider the transport (Eq. (2.1)) for the function

$$\phi(x, y) = \sin\left(\frac{\pi}{2}x\right)\sin\left(\frac{\pi}{2}y\right), \qquad (x, y) \in \Omega \equiv [0, 1]^2.$$

The velocity field is computed from the stream function $\psi = \frac{2U}{\pi}\phi$ to give

$$u_1(x, y) = \frac{\partial \psi}{\partial y}(x, y) = U \sin\left(\frac{\pi}{2}x\right)\cos\left(\frac{\pi}{2}y\right)$$

$$u_2(x, y) = -\frac{\partial \psi}{\partial x}(x, y) = -U \cos\left(\frac{\pi}{2}x\right)\sin\left(\frac{\pi}{2}y\right)$$

for all $(x, y) \in \Omega$. We define the Reynolds number as $\mathrm{Re} = \rho U / \Gamma_\phi$.

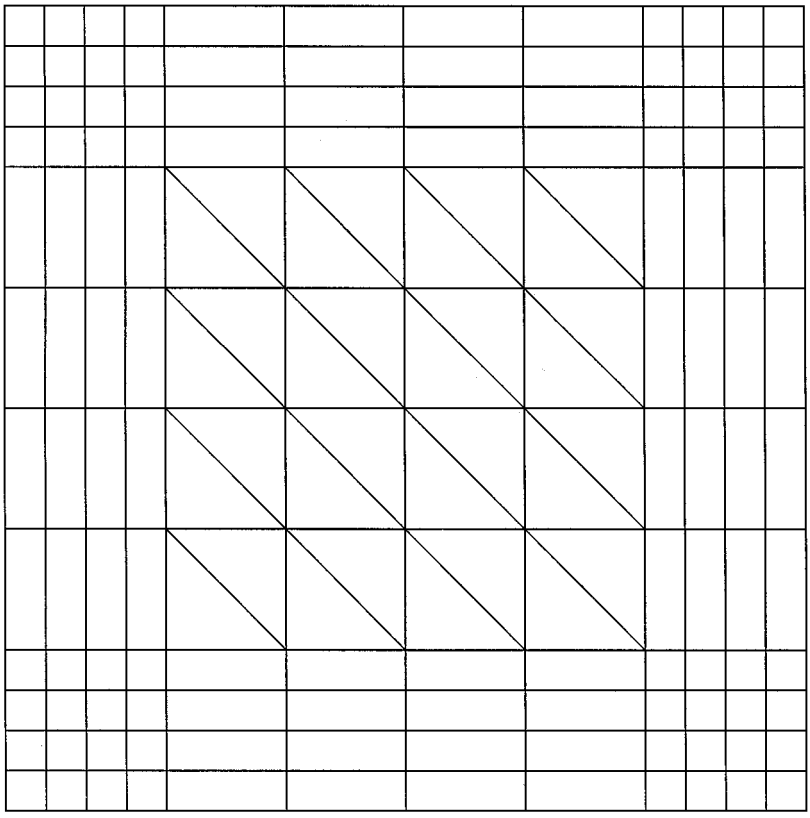

FIG. 4.1. Hybrid mesh comprising 160 elements.

The aim of this test case is to evaluate the influence of the boundary conditions on the quality of the results.

Since we know the analytical solution, we consider the following set of boundary conditions: (a) Dirichlet boundary condition at all boundaries, and (b) von Neumann boundary condition at all boundaries except at the inflow boundary for which Dirichlet boundary condition was used (the use of von Neumann conditions at all boundaries does not fix the solution). We consider hybrid grids comprising 160, 640, 2560, and 10,240 control volumes. Figure 4.1 shows the grid with 160 control volumes. The connection of the midpoints at the edges, as is shown in Fig. 4.2, generates all subsequent grids. For each grid, we also consider three values of the Reynolds number: $\mathrm{Re} = 1, 10, 10^6$. The reference values are $\ell_{\mathrm{ref}} = 1$ and $u_{\mathrm{ref}} = U$ (actually, we consider Eq. (2.1) in non-dimensional form, and then control the diffusive coefficient $1/\mathrm{Re}$). Figures 4.3a and 4.3b show the error evolution $\|e\|_\infty$ and $\|e\|_1$, respectively, as a function of the cell width. These figures clearly show that the magnitudes of the error $\|e\|_\infty$ (uniform) and $\|e\|_1$ decay quadratically for several Reynolds numbers under Dirichlet or von Neumann boundary conditions.

Viscous Flow through a Convergent Channel

In this second test case, we consider the analytical solution of the Navier–Stokes equations for the viscous incompressible fluid flow through a 2D convergent channel. The geometry of the problem is schematically shown in Fig. 4.4. At inlet and outlet, the values of the analytical

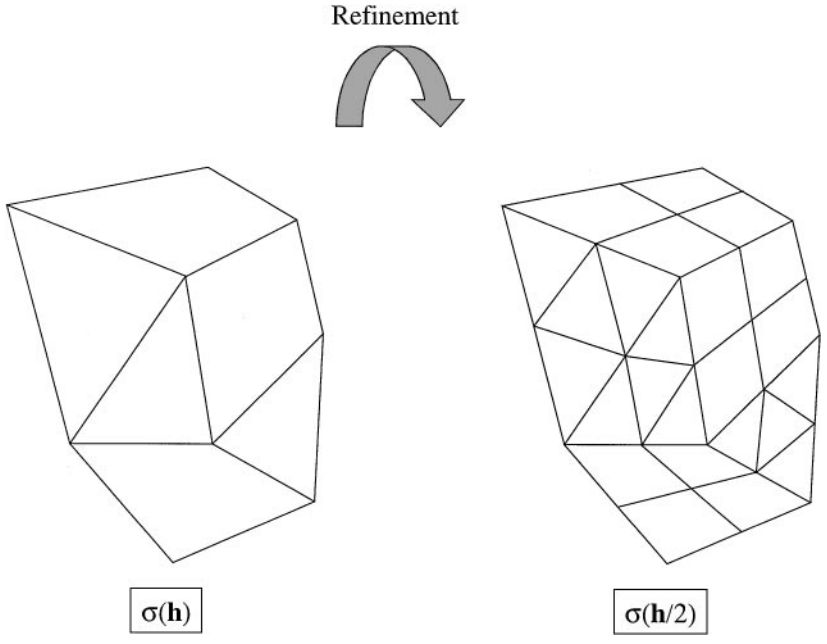

FIG. 4.2. Refinement strategy.

velocity field are prescribed, while the remaining boundary conditions correspond to the no-slip condition at the wall and symmetry condition at the centerline. The analytical solution for this problem can be found in, for example, Landau and Lifchitz [26] and is given in cylindrical coordinates (r, φ, z) as

$$v_\varphi = v_z = 0, \qquad v_r(r, \varphi) = \frac{6\nu}{r} f(\varphi),$$

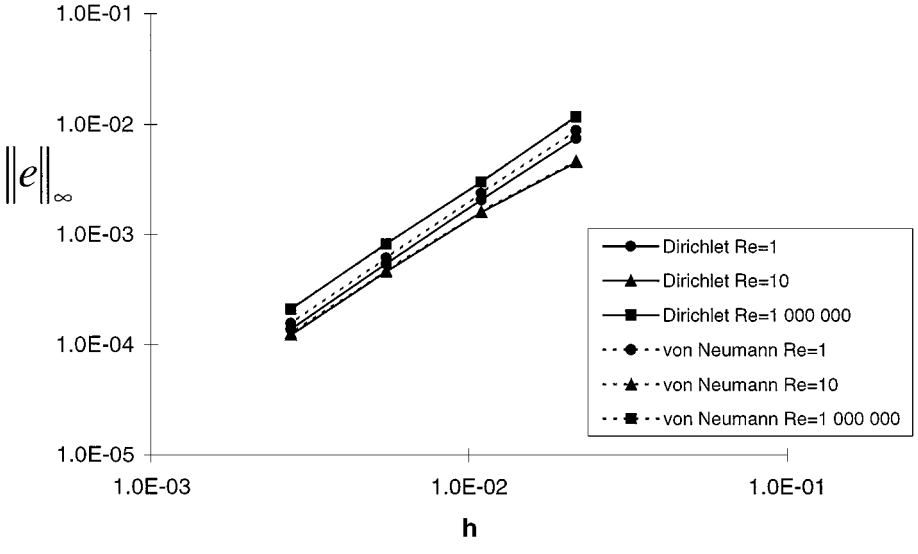

FIG. 4.3a. Error evolution ($\|e\|_\infty$) with mesh parameter.

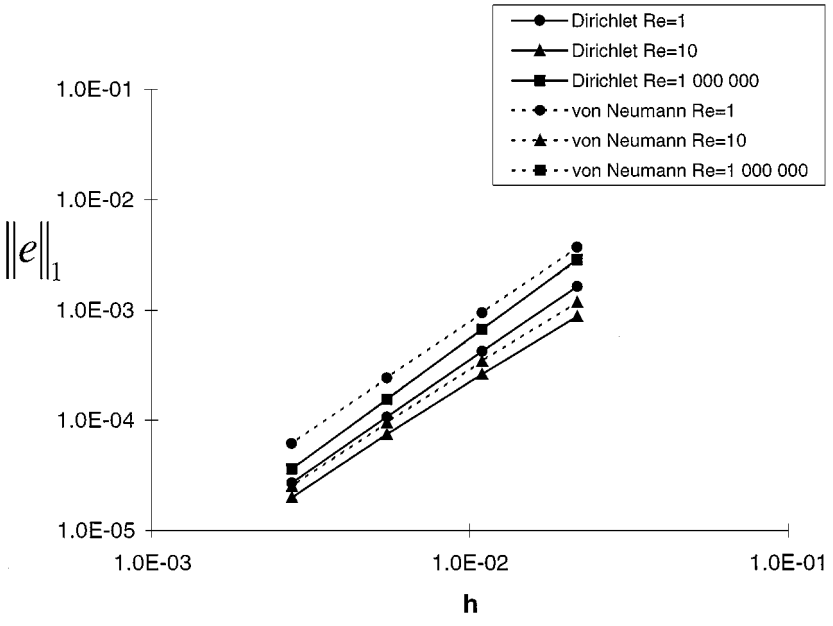

FIG. 4.3b. Error evolution ($\|e\|_1$) with mesh parameter.

where ν is the kinematic viscosity and $f(\varphi)$ is a function, which is implicitly given as

$$2\varphi = \int_{-u_0}^{f(\varphi)} \frac{dw}{\sqrt{(w+u_0)\left[-w^2-(1-u_0)w+q\right]}}, \tag{4.1}$$

where u_0 and q are constants which can be determined from the conditions

$$\alpha = \int_{-u_0}^{0} \frac{dw}{\sqrt{(w+u_0)\left[-w^2-(1-u_0)w+q\right]}}$$

$$\frac{\mathrm{Re}}{6} = \int_{-u_0}^{0} \frac{w\,dw}{\sqrt{(w+u_0)\left[-w^2-(1-u_0)w+q\right]}},$$

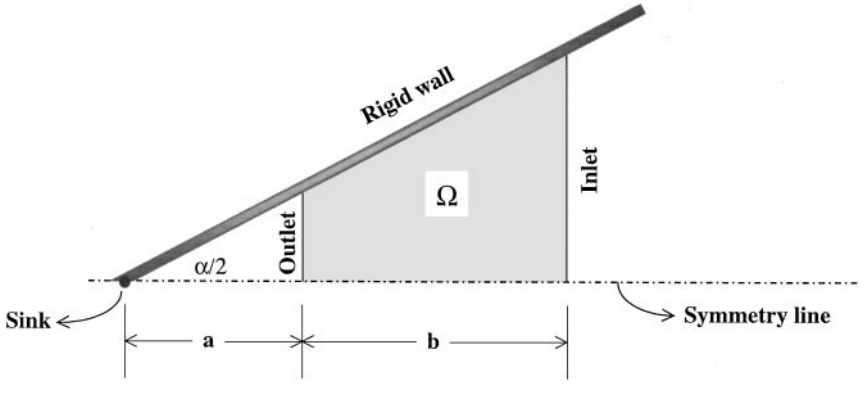

FIG. 4.4. Problem configuration.

where α is the aperture angle (see Fig. 4.4) and Re is the Reynolds number $\mathrm{Re} = \frac{|Q|}{\nu\rho}$, Q being the mass flow rate through the convergent channel. Equation (4.1) can also be written as

$$2\varphi = \Xi(f(\varphi)) - \Xi(u_0),$$

where

$$\Xi(x) = \Xi_m(x) F\left(\sin^{-1}\left(\frac{\sqrt{\frac{1+2x-u_0+\sqrt{4q+(u_0-1)^2}}{\sqrt{4q+(u_0-1)^2}}}}{\sqrt{2}}\right), \frac{2\sqrt{4q+(u_0-1)^2}}{\left(1-3u_0+\sqrt{4q+(u_0-1)^2}\right)}\right)$$

and

$$\Xi_m(x) = \frac{2\sqrt{2}\left[x+\frac{1}{2}\left(1-u_0+\sqrt{4q+(u_0-1)^2}\right)\right]\sqrt{\left(-1-2x+u_0+\sqrt{4q+(u_0-1)^2}\right)}}{\sqrt{[q+x(u_0-1-x)]\left(1+2x-u_0+\sqrt{4q+(u_0-1)^2}\right)\left(1-3u_0+\sqrt{4q+(u_0-1)^2}\right)}}.$$

In the above expression $F(x;m)$ stands for the elliptic integral of first kind. We consider four meshes comprising 106, 428, 1720, and 6896 control volumes. Figure 4.5 shows the grid comprising 1720 control volumes. The values of the parameters used in the simulations are $\mathrm{Re} = 600$, $\alpha = 30^\circ$, $a = b = 1$, $\rho = 1$, $\nu = 1.33 \times 10^{-3}$,

$$\ell_{\mathrm{ref}} = (a+b)\tan\left(\frac{\alpha}{2}\right), \qquad u_{\mathrm{ref}} = |Q|/\rho\ell_{\mathrm{ref}}.$$

The aim of this test case is to verify the order of accuracy of the method for both the velocity vector and pressure fields, and to compare their error evolution with the first-order

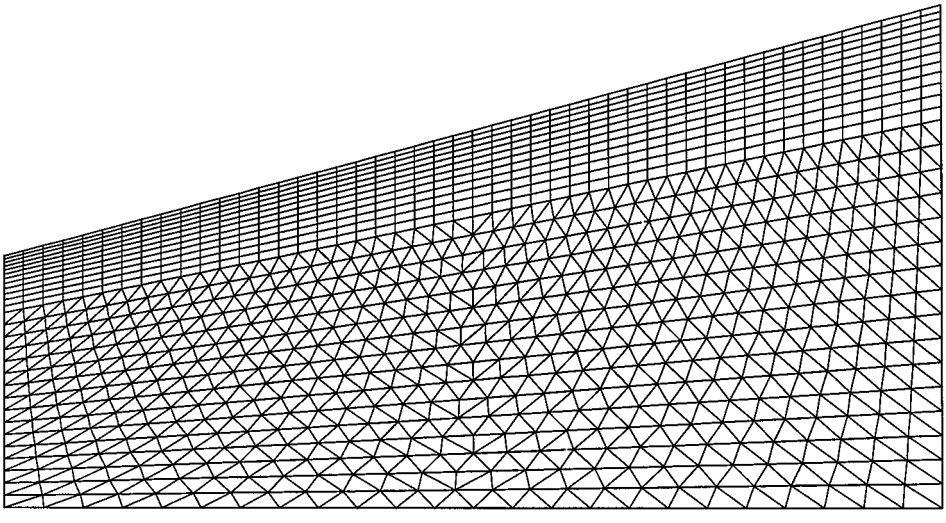

FIG. 4.5. Hybrid mesh comprising 1720 elements.

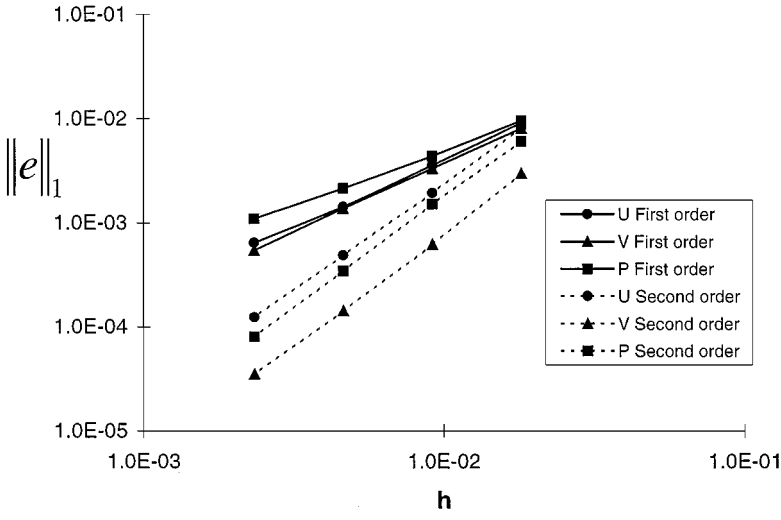

FIG. 4.6. Error evolution ($\|e\|_1$) with mesh parameter.

upwind scheme. Figure 4.6 shows the error evolution, $\|e\|_1$, of the velocity vector and pressure fields as a function of the cell width for both first- and second-order schemes. The results show the quadratic evolution of the error norm for the proposed second-order scheme while, as expected, the first-order scheme displays linear error evolution. The proposed second-order-accurate scheme clearly shows that for the same level of accuracy, it requires many fewer mesh nodes than the first-order-accurate scheme and that this tendency increases with accuracy requirement.

Figures 4.7a, 4.7b, and 4.7c show the comparison between analytical and predicted solutions of u_1, u_2, and p, respectively, along the vertical coordinate at $x = 1.5$. The predicted profiles, obtained with 6896 control volumes, are virtually identical to the analytical solution.

Figure 4.8a shows the predicted pressure field before the reconstruction procedure. This solution displays the checkerboard mode obtained with a mesh comprising only quadrilaterals with about 600 elements. This problem can be eliminated (see Fig. 4.8b), with the reconstruction procedure explained in Section 3.

Analytical Cavity

In this third test case, we consider the recirculating viscous flow in a square cavity driven by combined shear and body forces. Figure 4.9 shows schematically the geometry of the problem and boundary conditions for the velocity field. This benchmark appeared in Shih *et al.* [27], where the details of the problem can also be found. Here we summarize the relevant information. The vertical body force is given by the expression

$$B(x_1, x_2; \mathrm{Re}) = \frac{8}{\mathrm{Re}}\left[24 \int \zeta_1(x_1) + 2\zeta_1'(x_1)\zeta_2''(x_2) + \zeta_1'''(x_1)\zeta_2(x_2)\right]$$
$$- 64[Y_2(x_1)Y_3(x_2) - \zeta_2(x_2)\zeta_2'(x_2)Y_1(x_1)],$$

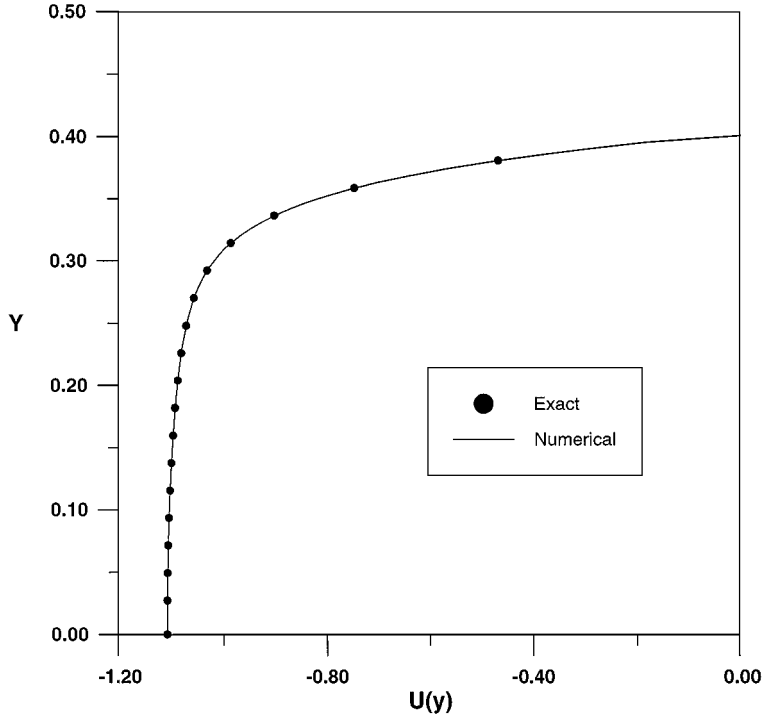

FIG. 4.7a. u_1-profile: exact vs numerical.

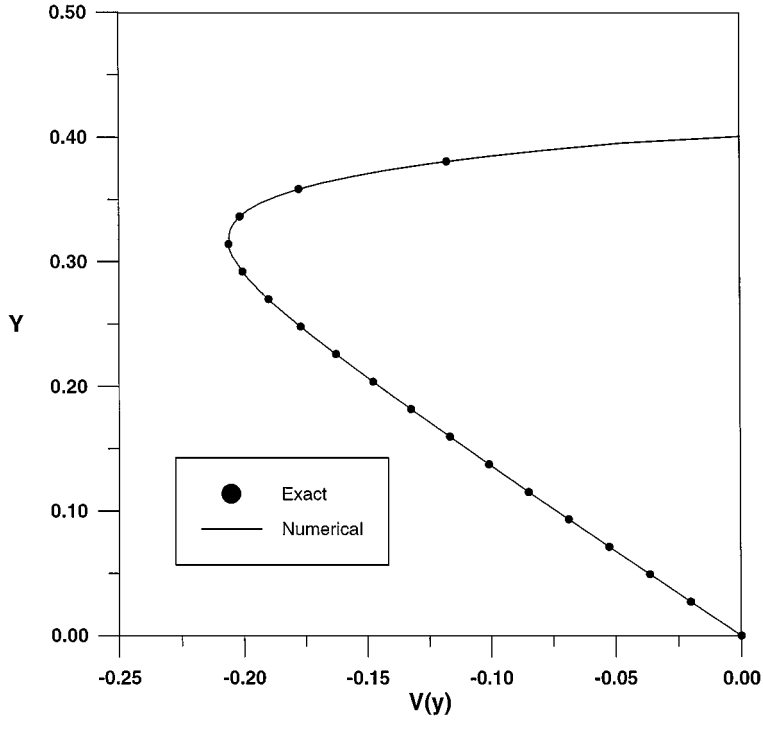

FIG. 4.7b. u_2-profile: exact vs numerical.

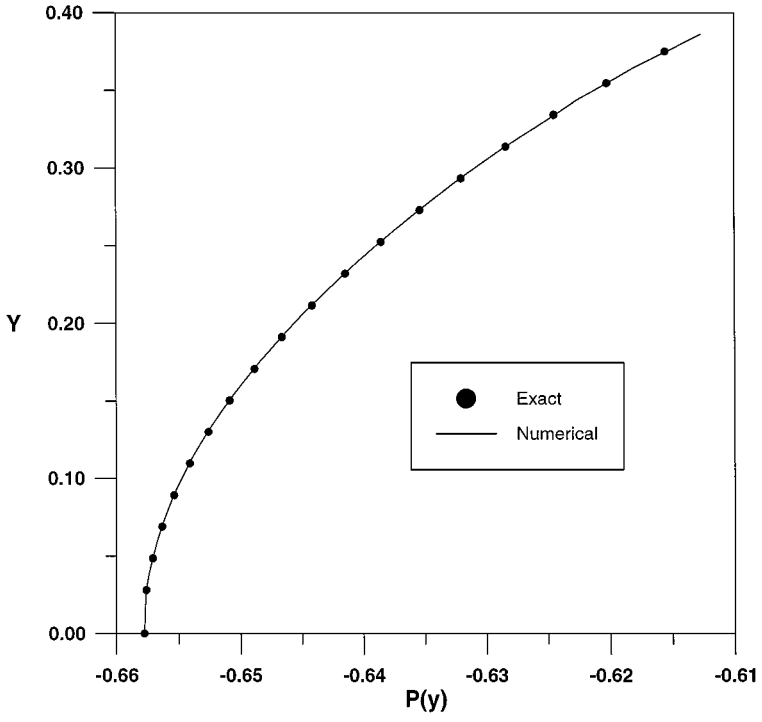

FIG. 4.7c. *p*-profile: exact vs numerical.

where

$$\zeta_1(x_1) = x_1^4 - 2x_1^3 + x_1^2$$
$$\zeta_2(x_2) = x_2^4 - x_2^2$$
$$Y_1(x_1) = \zeta_1(x_1)\zeta_1''(x_1) - [\zeta_1'(x_1)]^2$$
$$Y_2(x_1) = \int \zeta_1(x_1)\zeta_1'(x_1)$$
$$Y_3(x_2) = \zeta_2(x_2)\zeta_2'''(x_2) - \zeta_2'(x_2)\zeta_2''(x_2)$$

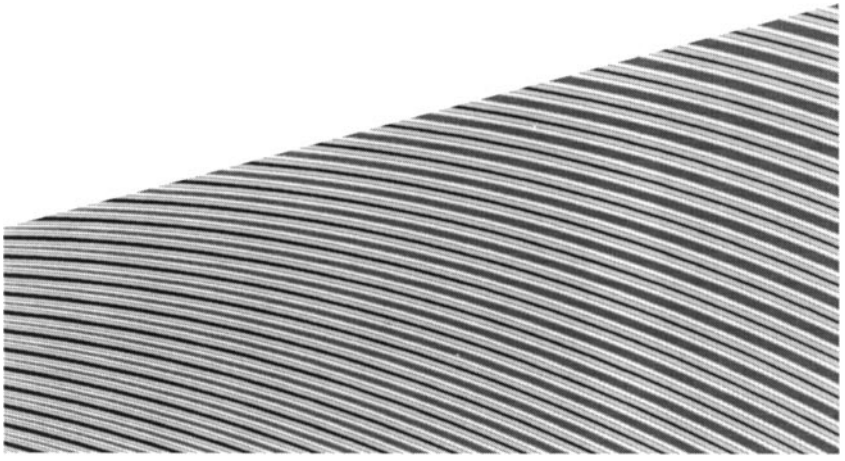

FIG. 4.8a. Pressure field: with checkerboard.

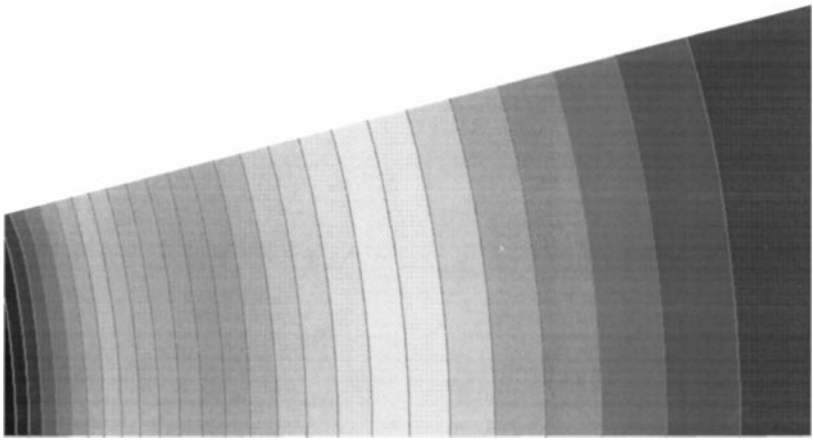

FIG. 4.8b. Pressure field: reconstructed.

for all $(x_1, x_2) \in \Omega \equiv [0, 1]^2$. The Dirichlet boundary conditions correspond to zero velocity at all boundaries except for the top surface, where

$$u_1(x_1, 1) = 16\zeta_1(x_1), \qquad x_1 \in [0, 1].$$

An exact solution for this problem exists and is known to be

$$u_1(x_1, x_2) = 8\zeta_1(x_1)\zeta_2'(x_2)$$
$$u_2(x_1, x_2) = -8\zeta_1'(x_1)\zeta_2(x_2)$$

and

$$p(x_1, x_2; \mathrm{Re}) = \frac{8}{\mathrm{Re}}\left[24\left(\int \zeta_1(x_1)\right)\zeta_2'''(x_2) + 2\zeta_1'(x_1)\zeta_2'(x_2)\right] + 64Y_2(x_1)\left\{\zeta_2(x_2)\zeta_2''(x_2) - [\zeta_2(x_2)]^2\right\}.$$

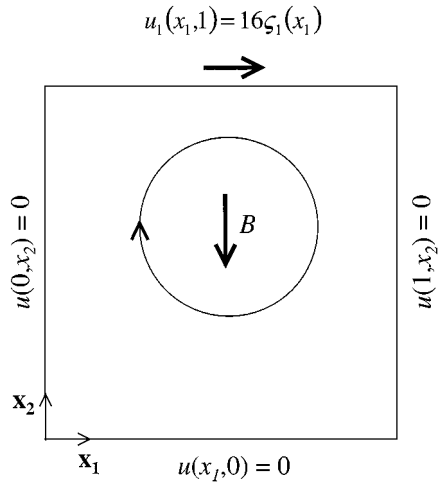

FIG. 4.9. Problem configuration.

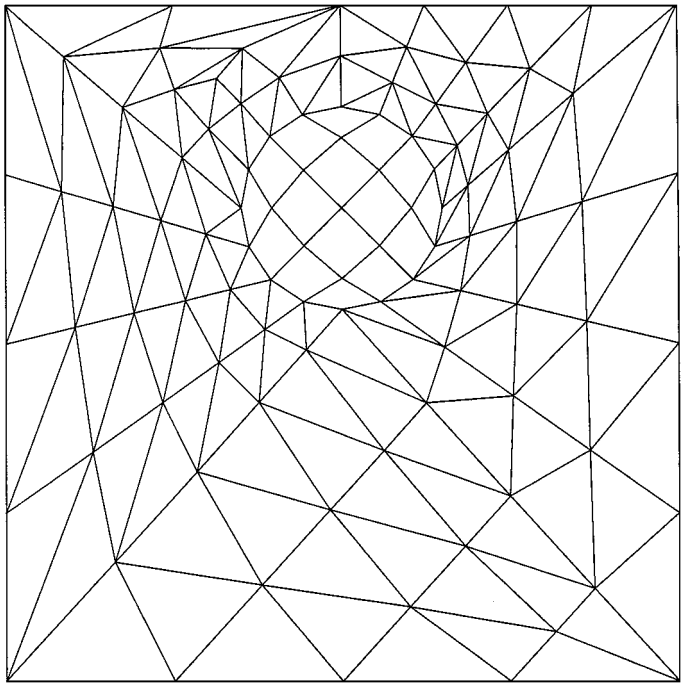

FIG. 4.10. Hybrid mesh comprising 160 elements—highly irregular.

We compute this problem using three pairs of grids. Each pair comprises about 160, 630, and 2500 control volumes. The intent of this test case is to assess the influence of the grid irregularity on the quality of the numerical results. Figure 4.10 depicts the irregular grid comprising 160 control volumes; the regular grid is the same as in Fig. 4.1. The pertinent parameters for the simulation are $\mathrm{Re} = 1$, $u_{\mathrm{ref}} = \ell_{\mathrm{ref}} = 1$. Figure 4.11 displays the error norms of the predicted velocity components for the different grids and clearly shows that the numerical solution is second order accurate.

Classical Lid-Driven Cavity

As the final test case, we consider the classical benchmark of the lid-driven cavity flow. The boundary conditions are similar to those of the previous test case except for the upper boundary for which a constant unit velocity is assigned. The solutions of Ghia [28], obtained using a second-order-accurate numerical method and a very fine mesh at $\mathrm{Re} = 100$ and $\mathrm{Re} = 1000$, are taken as reference values. For this test case we use $u_{\mathrm{ref}} = \ell_{\mathrm{ref}} = 1$.

Figure 4.1 shows a typical grid used in the calculations and Fig. 4.12 depicts the streamlines evaluated from the predicted velocity field at $\mathrm{Re} = 1000$ using 10,240 mesh control volumes. Prior to the comparison between the predicted and the reference velocity values, a systematic assessment of the influence of several model parameters is performed. Figures 4.13a and 4.13b show, for $\mathrm{Re} = 100$ and $\mathrm{Re} = 1000$, respectively, the required number of iterations to achieve steady state of the discrete Navier–Stokes equations, as a function of the under-relaxation factor for the pressure evolution (Eq. (3.28)) and CFL parameter. The solid and dash lines denote coarse (640 elements) and finer (2560 elements) meshes, respectively. The figures indicate that the most efficient relaxation parameter corresponds to $\alpha_p = 1$. This represents a clear gain in numerical efficiency over semi-implicit

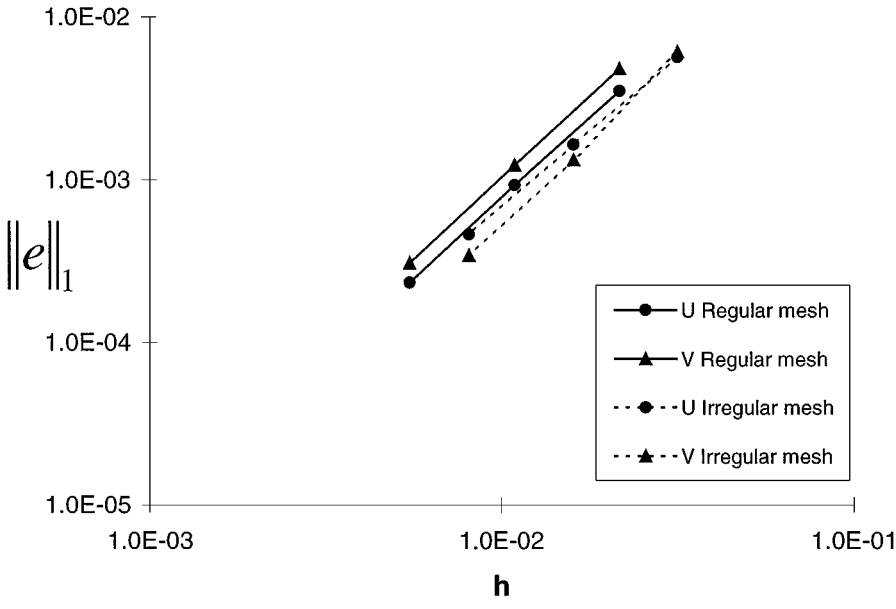

FIG. 4.11. Error evolution ($\|e\|_1$) with mesh parameter.

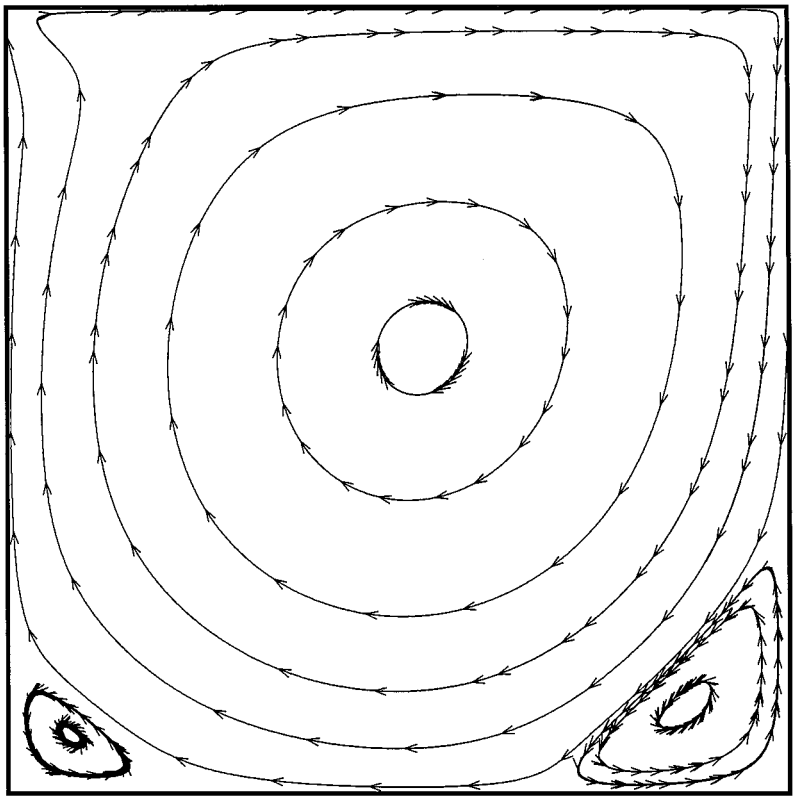

FIG. 4.12. Streamlines for lid-driven cavity Re = 1000.

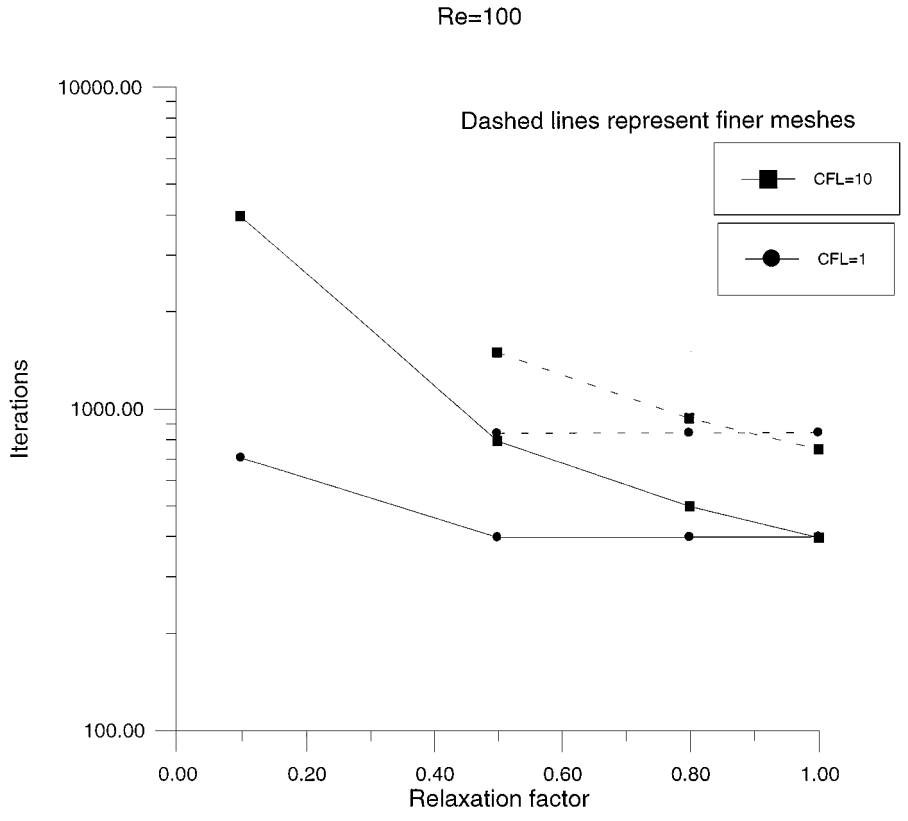

FIG. 4.13a. Iterations vs relaxation factor Re = 100.

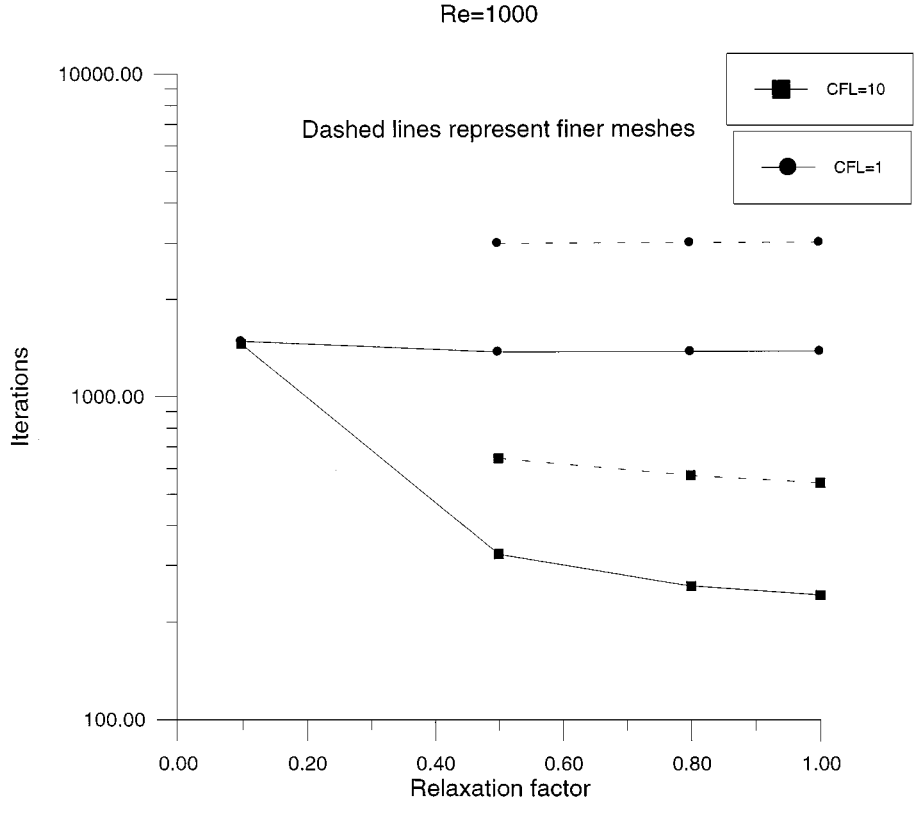

FIG. 4.13b. Iterations vs relaxation factor Re = 1000.

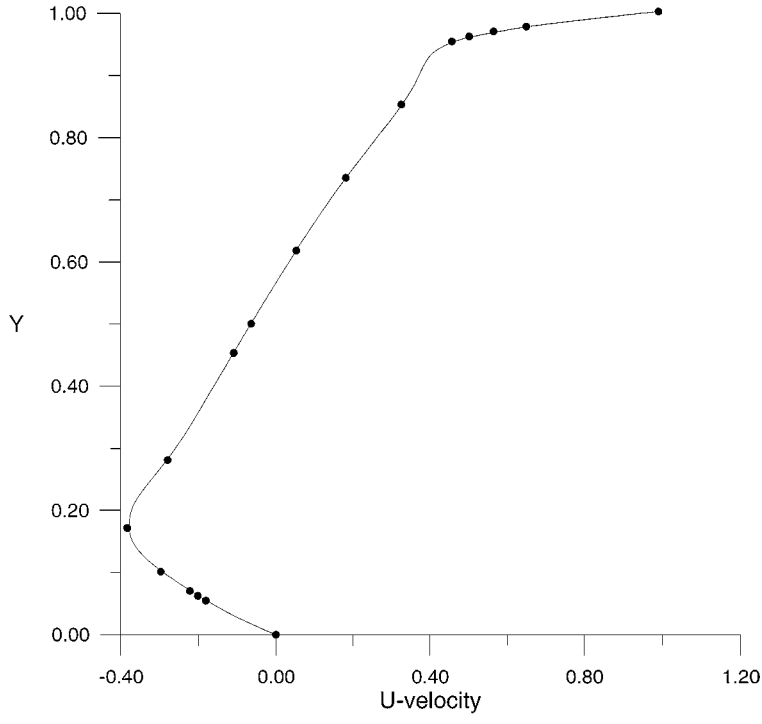

FIG. 4.14a. u_1-profile: reference (Ghia *et al.*) vs actual predictions.

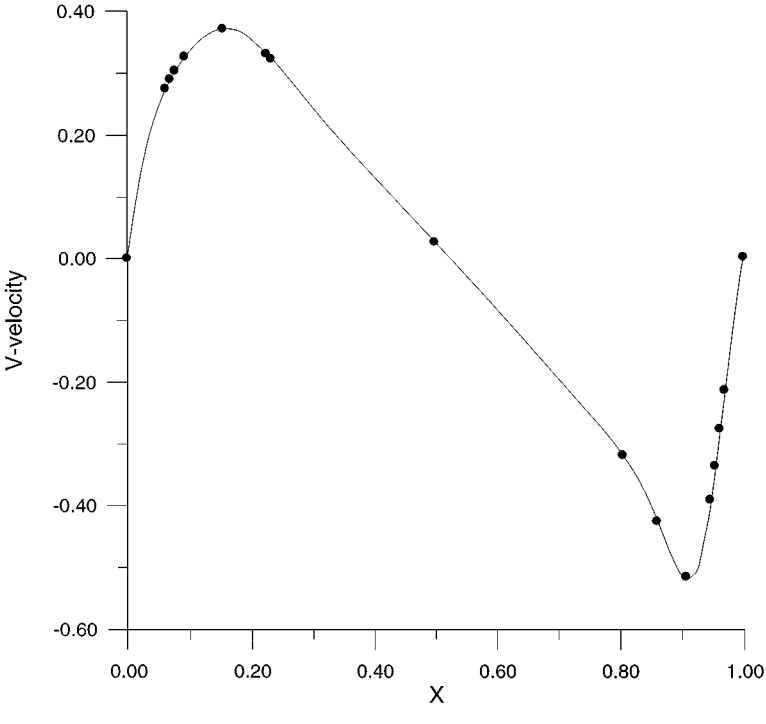

FIG. 4.14b. u_2-profile: reference (Ghia *et al.*) vs actual predictions.

pressure-linked equations (SIMPLE) extensions used in the framework of unstructured grids for which a strong under-relaxation may be required. Another conclusion that can be drawn from the results is related to the value of CFL parameter used in the fractional time step projection method. Numerical experimentation with the present flow configuration shows the optimum value to be around 10. Also, this choice is independent of the Reynolds number and cell width.

Finally, Figs. 4.14a and 4.14b show the axial and transversal velocity components profiles across the center plane of the cavity for $\mathrm{Re} = 1000$, obtained with the above mesh with 10,240 control volumes. The numerical solutions obtained with the ULSS are virtually identical to the reference values of Ghia *et al.* [28] (with a 128×128 uniform mesh).

5. CONCLUSIONS

In this paper, a new finite-volume projection method for incompressible fluid flow has been presented. The method is second-order accurate in general irregular unstructured hybrid grids. This was achieved by choosing a grid staggering that allows one to naturally define the relevant Hilbert spaces and the gradient and divergence operators. In particular, we do not fix one of the operators and define the other to be skew adjoint of the first.

Numerical simulation of different test cases showed that the combination of the method with the upwind least squares convection discretization scheme yields second-order global accuracy and it is in agreement with the theoretical analysis undertaken along with the presentation of the method. The results show that the present method yields a second-order-accurate solution for the incompressible steady version of the Navier–Stokes equations on arbitrary unstructured hybrid meshes for a broad range of two-dimensional geometries and Reynolds numbers.

To the authors' knowledge, this paper represents the first general unstructured grid finite volume method to achieve full second-order accuracy for the steady incompressible 2D version of Navier–Stokes equations.

REFERENCES

1. F. H. Harlow and J. E. Welch, Numerical calculation of time-dependent viscous incompressible flow of fluid with free surface, *Phys. Fluids* **8**, 2182 (1965).
2. C. W. Hirt, A. A. Amsden, and J. L. Cook, An arbitrary Lagrangean–Eulerian computing method for wall flow, *J. Comput. Phys.* **14**, 227 (1974).
3. A. J. Chorin, A numerical method for solving incompressible viscous flow problems, *J. Comput. Phys.* **2**, 12 (1967).
4. S. V. Patankar and D. B. Spalding, A calculation procedure for heat, mass and momentum transfer in three dimensional parabolic flows, *Int. J. Heat Mass Transfer* **15**, 1787 (1972).
5. C. M. Rhie and W. L. Chow, Numerical study of the turbulent flow past in airfoil with trailing edge separation, *AIAA J.* **21**, 1525 (1983).
6. J. H. Ferziger and M. Perić, *Computational Method for Fluid Dynamics* (Springer-Verlag, Berlin/New York, 1996).
7. R. Sani, P. Gresho, R. Lee, D. Griffiths, and M. Engelman, The cause and cure (?) of the spurious pressure generated by certain FEM solutions of the incompressible Navier–Stokes equations, *Int. J. Numer. Methods Fluids* **1**, 17 (1981).
8. A. J. Chorin, Numerical solution of the Navier–Stokes equations, *Math. Comput.* **22**, 745 (1968).

9. A. J. Chorin, On the convergence of discrete approximations of the Navier–Stokes equations, *Math. Comput.* **23**, 341 (1969).
10. J. Van Kan, A second-order accurate pressure-correction scheme for viscous incompressible flow, *SIAM J. Sci. Statist. Comput.* **7**, 12 (1986).
11. J. B. Bell, P. Colella, and H. M. Glaz, A second-order projection method for the incompressible Navier–Stokes equations, *J. Comput. Phys.* **85**, 257 (1989).
12. J. B. Bell, J. M. Solomon, and W. G. Szymczak, Projection method for viscous incompressible flow on quadrilateral grids, *AIAA J.* **32**, 1961 (1994).
13. A. S. Almgren, J. B. Bell, and W. G. Szymczak, A numerical method for the incompressible Navier–Stokes equations based on an approximate projection, *SIAM J. Sci. Comput.* **17**, 358 (1996).
14. J. L. Guermond and L. Quartapelle, Calculation of incompressible viscous flows by an unconditionally stable projection FEM, *J. Comput. Phys.* **132**, 12 (1997).
15. P. M. Gresho, On the theory of semi-implicit projection methods for viscous incompressible flow and its implementation via a finite element method that also introduces a nearly consistent mass matrix. 1. Theory, *Int. J. Numer. Methods Fluids* **11**, 587 (1990).
16. P. M. Gresho and S. T. Chan, On the theory of semi-implicit projection methods for viscous incompressible flow and its implementation via a finite element method that also introduces a nearly consistent mass matrix. 2. Implementation, *Int. J. Numer. Methods Fluids* **11**, 621 (1990).
17. P. D. Lax, *Hyperbolic Systems of Conservation Laws and the Mathematical Theory of Shock Waves* (SIAM, Philadelphia, 1990).
18. A. Harten, B. Engquist, S. Osher, and S. R. Chakravarthy, Uniformly high order accuracy essentially non-oscillatory schemes, III, *J. Comput. Phys.* **71**, 231 (1987).
19. B. van Leer, Towards the ultimate conservative difference scheme. V. A second-order sequel to Godunov's method, *J. Comput. Phys.* **32**, 101 (1979).
20. A. Harten and S. Osher, Uniformly high order accurate non-oscillatory schemes, I, *SIAM J. Numer. Anal.* **24**, 279 (1987).
21. T. Hayase, J. A. C. Humphrey, and R. Greif, A consistently formulated quick scheme for fast and stable convergence using finite-volume iterative calculation procedure, *J. Comput. Phys.* **98**, 108 (1992).
22. M. Perić, *A Finite-Volume Method for the Prediction of Three-Dimensional Fluid Flow in Complex Ducts* (Ph.D. thesis, Imperial College of London, 1985).
23. S. A. Orzag, Spectral methods for problems in complex geometries, *J. Comput. Phys.* **37**, 70 (1980).
24. H. A. van der Vorst, BI-CGSTAB: A fast and smoothly converging variant of bicg for the solution of non-symmetric linear systems, *SIAM J. Statist. Comput.* **13**, 631 (1992).
25. R. I. Issa, Solution of the implicitly discretized fluid flow equations by operator splitting, *J. Comput. Phys.* **62**, 40 (1985).
26. L. Landau and E. Lifchitz, *Mécanique des fluides* (Mir, Moscow, 1989).
27. T. M. Shih, C. H. Tan, and B. C. Hwang, Effects of grid staggering on numerical schemes, *Int. J. Numer. Methods Fluids* **9**, 193 (1989).
28. U. Ghia, K. N. Ghia, and C. T. Shin, High-Re solutions for incompressible flow using the Navier–Stokes equations and a multigrid method, *J. Comput. Phys.* **48**, 387 (1982).